

STRUCTURAL, OPTICAL, AND VIBRATIONAL CHARACTERIZATIONS OF NdAlO₃ MATERIALS

M.Sc. Thesis

by

VIKASH KUMAR SINGAR



DISCIPLINE OF PHYSICS
INDIAN INSTITUTE OF TECHNOLOGY INDORE
JUNE 2023

STRUCTURAL, OPTICAL, AND VIBRATIONAL CHARACTERIZATIONS OF
NdAlO₃ MATERIALS

THE THESIS

Submitted in partial fulfillment of the
requirements for the award of the degree

of

Master of Science

by

VIKASH KUMAR SINGAR



DISCIPLINE OF PHYSICS
INDIAN INSTITUTE OF TECHNOLOGY INDORE
JUNE 2023

*



INDIAN INSTITUTE OF TECHNOLOGY INDORE

CANDIDATE'S DECLARATION

I hereby certify that the work which is being presented in the thesis entitled '**STRUCTURAL, OPTICAL, AND VIBRATIONAL CHARACTERIZATIONS OF PEROVSKITE MATERIALS**' in the partial fulfillment of the requirements for the award of the degree of **MASTER OF SCIENCE** and submitted in the **DISCIPLINE OF PHYSICS, Indian Institute of Technology Indore** is an authentic record of my own work carried out during the time period from July 2022 to June 2023 under the supervision of Prof. Pankaj R. Sagdeo, Professor, Department of physics, IIT Indore.

The matter presented in this thesis has not been submitted by me for the award of any other degree of this or any other institute.

Signature of the student with the date

VIKASH KUMAR SINGAR

This is to certify that the above statement made by the candidate is correct to the best of my/our knowledge.

Signature of the Supervisor of

M.Sc. thesis #1 (with date)

(Prof. Pankaj R. Sagdeo)

Vikash Kumar Singar has successfully given his/her M.Sc. _____.

Signature(s) of Supervisor(s) of MSc Thesis

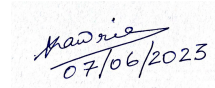
Convener, DPGC

Date:



Signature of PSPC Member #1

Date: 06.06.2023



Signature of PSPC Member #2

Date:

Dedicated To
My Parents
And Teachers

ACKNOWLEDGEMENTS

I would like to extend my heartfelt gratitude to my thesis advisor, Prof. Pankaj R. Sagdeo, for his unwavering support throughout my M.Sc. project. His continuous guidance, motivation, and vast knowledge have been instrumental in shaping my research, studies, and the completion of this thesis.

In addition to my advisor, I would like to express my appreciation to my PSPC committee members: Prof. Krushna R. Mvani and Dr. Alestin Mawrie, for their valuable support and encouragement during this journey. I am extremely thankful to the Physics Department of IIT Indore for providing me with the necessary facilities that were crucial for the successful execution of my research.

I am sincerely grateful to Dr. Archana Sagdeo, Scientific Officer-F at RRCAT, Indore, for her generous support and for granting us access to the X-ray diffraction facilities in her lab. I would also like to express my deep appreciation to Dr. Archana Sagdeo for introducing me to the world of synchrotrons and providing me with a comprehensive understanding of their functioning. Thank you so much for your guidance.

My heartfelt thanks go to Dr. Minal Gupta and Ms. Ritu Nain, whose assistance has been invaluable in helping me learn various sample preparation techniques. I would also like to acknowledge the kind support and assistance provided by Mr. Omkar Rambadey and Dr. Minal Gupta, which played a significant role in the successful completion of my project.

I sincerely thank all the lab members, namely Mr. Omkar Rambadey, Mr. Kailash Kumar, Dr. Minal Gupta, and Ms. Ritu Nain, for fostering a friendly and nurturing environment. Working alongside them has been a privilege and an enriching experience. I would also like to express my gratitude to all my friends for their cooperation and support.

Lastly, I would like to express my gratitude to you for your invaluable assistance and insightful comments. Our discussions have been truly

enlightening, and your guidance has kept me motivated and inspired to work harder.

Vikash Kumar Singar

Abstract

The present work demonstrates the tuning of *f*-orbital crystal field splitting in the NdAlO₃ rare-earth aluminate system by La-substitution. The polycrystalline samples of pure and La-substituted NdAlO₃ have been synthesized using the sol-gel synthesis method. The purity of the rhombohedral phase of Nd_{1-x}La_xAlO₃ ($x = 0, 0.1, 0.2, 0.3, 0.4, 0.5$) samples have been confirmed via X-ray diffraction studies. The effect of the ionic radius of La at the Nd site has been observed in structural and optical properties. The structural distortion due to an increase in ionic radii of La-cation has been realized in terms of systematic increment in the lattice parameter, Nd/La–O bond length, and Nd/La–O–La/Nd bond angle. Further, in order to observe the *f*-*f* transitions, optical absorption spectroscopy experiments have been performed for Nd_{1-x}La_xAlO₃ samples in diffuse reflectance mode. The observed crystal field transitions related to Nd-cation seen in optical spectra show systematic variation with increasing La-substitution. These variations have been understood by correlating the difference in change transition

energy (E_2-E_1) with Nd/La-O bond length. This study has proven the potential for optical absorption spectroscopy in detecting and tuning of crystal field transitions. In order of further investigate the crystal field splitting of the considered system, theoretical work in PyCrystalfield Software and Simpre Software has been done.

TABLE OF CONTENTS

LIST OF FIGURES

LIST OF TABLES

Chapter 1: Introduction

1.1 History of perovskite material	(1)
1.2 ABO ₃ -type perovskite oxide	(2)
1.3 Goldschmidt Tolerance factor	(5)
1.4 Neodymium aluminate (NdAlO ₃)	(5)
1.5 Crystal field transition	(6)
1.5.1 Crystal field transitions in various oxides	(7)
1.6 Selection of Dopant	(10)

Chapter 2: Experimental section

2.1 Sample synthesis via Sol-gel synthesis technique ...	(12)
2.2 X-ray diffraction	(14)

2.3 Diffused Reflectance Spectroscopy (18)

2.2.3 Raman Spectroscopy (24)

Chapter 3: Results and Discussion

3.1 Structural characterization using X-ray diffraction (28)

3.2 Optical absorption spectroscopy (34)

Chapter 4: Theoretically work.

4.1 The parametric Modal Hamiltonian (42)

4.2 PyCrystalfield Software (49)

Chapter 5: Thesis Conclusion and Future Scope(54)

REFERENCES(55)

LIST OF FIGURES

Chapter 1

Figure 1.1: Schematic diagram of ABO_3 .

Figure 1.2: ABO_3 type perovskite materials.

Figure 1.3: Splitting of f-orbital under the crystal field in Tm^{3+} ion system, and Nd^{3+} based system.

Figure 1.4: Optical absorption spectra of Nd-doped Yttrium Aluminate Garnet, and Nd-doped Aluminum Oxide.

Chapter 2

Figure 2.1: Diffraction of X-ray by a crystal.

Figure 2.2: Schematic diagram of X-ray Diffractometer.

Figure 2.3: Schematic diagram of Specular and Diffuse Reflection.

Figure 2.4: Schematic diagram for the Kubelka-Munk analysis of reflectance and transmittance of a scattering medium.

Figure 2.5: Experimental set up for diffuse reflectance measurement, (a) Carry 60 UV-Visible Spectrometer, (b) Internal set up of UV-Visible spectrometer.

Figure 2.6: Schematic representation of Raman Scattering.

Figure 2.7: Raman Spectrometer.

Chapter 3

Figure 3.1: (a): X-ray diffraction data of pure and La-substituted NAO system. (b): Rietveld refinement pattern for La; NAO using space group R-3c.

Figure 3.2: (a): Magnified view of X Ray-Diffraction of La-substituted NdAlO₃. (b): Variation of Lattice parameter.

Figure 3.3: Optical absorption spectra of La-substituted NdAlO₃ showing crystal field transitions.

Figure 3.4: Magnified view of crystal field transitions that are tuned by the La-incorporation in the NdAlO₃ host-lattice.

Figure 3.5: The Tauc plot for bandgap calculations.

Figure 3.6: Energy difference ($\Delta E = E_2 - E_1$) vs bond length (Nd/La-O₂).

Chapter 4

Figure 4.1: PyCrystalfield workflow. One can begin either with a .cif file or a list of CEF parameters, and then calculate a point charge model or a CEF Hamiltonian respectively.

Figure 4.2: Variation of transition energy and bond length.

LIST OF TABLES

Table 2.1: Variation of transition energy and bond length.

Table 3.1: Crystallographic information extracted from Rietveld refinement method with

space group R-3c:

Table 3.2: Variation of transition energy and bond length.

Table 4.1: Ground state energy of Nd-ions.

Table 4.2: The relation between change transition energy and bond length.

Chapter 1

Introduction

1.1 History of perovskite material:

The rapid progress in the field of perovskite materials has led to a significant amount of research and development, as well as commercial interest from companies looking to bring perovskite-based products to market.¹ However, there are still challenges to be addressed in terms of the stability and scalability of perovskite materials, and ongoing research efforts are focused on addressing these issues. Perovskite materials have a unique crystal structure, which was named after the mineral perovskite (CaTiO_3) - a calcium titanate-based mineral.² The mineral was discovered in the Ural Mountains of Russia by Gustav Rose, a German scientist, during a trip to Russia in 1839.² It was named 'perovskite' after the Russian mineralogist Lev Aleksevich von Perovski.³ In the 1990s, perovskite materials began to attract significant attention in the field of solid-state electronics due to their interesting properties, such as high-temperature superconductivity.⁴ Today, researchers have started exploring the use of perovskite materials for photovoltaic applications.^{5,6} One category of layered perovskite derivatives that has gained increasing research attention is the Ruddlesden–Popper (RP) perovskites.⁷ They have a general formula of $\text{A}_{n+1}\text{B}_n\text{X}_{3n+1}$ or $\text{AX}(\text{ABX}_3)_n$, where $n = 1, 2, 3$, and so on. RP perovskites consist of alternating rock-salt layers (AX) and perovskite-like layers (ABX₃) along the crystallographic c-axis direction.⁷ The positive integer n represents the number of consecutive perovskite-like layers, consisting of corner-sharing BX_6 octahedra, that are sandwiched between two rock-salt layers.⁷ Currently, RP phases with single ($n = 1$), double ($n = 2$), or triple ($n = 3$) perovskite layers are the most widely studied. As n approaches infinity ($n \rightarrow \infty$), it corresponds to the well-known simple perovskite phase (ABX_3 , where X= oxygen anion).⁷

1.2 ABO₃-type perovskite material:

The perovskite family is one of the most important representatives among a large variety of inorganic compounds.⁸ The ABO₃-type compounds with the perovskite structure are constituted by most of the chemical elements from the periodic table that majorly involve transition metal elements, however, this range also extends to group IIIA elements, viz., gallates, indates, and so forth.^{3,9} The diversity of elements that form perovskite structures and their ability to create cation- or anion-deficient structures shows an extremely broad range of physical and chemical properties.⁹ ABO₃ perovskites-based oxide system in different fields with wide applications in energy storage devices¹⁰, electrode and electrolyte material in fuel cells¹¹, magnetism¹², ferroelectrics¹³, redox reaction¹⁴, etc. Most of the physical properties of ABO₃ perovskite material, including structural distortion of the lattice, band structure, vibrational properties, etc., are governed by the tilting of BO₆ octahedra⁹.

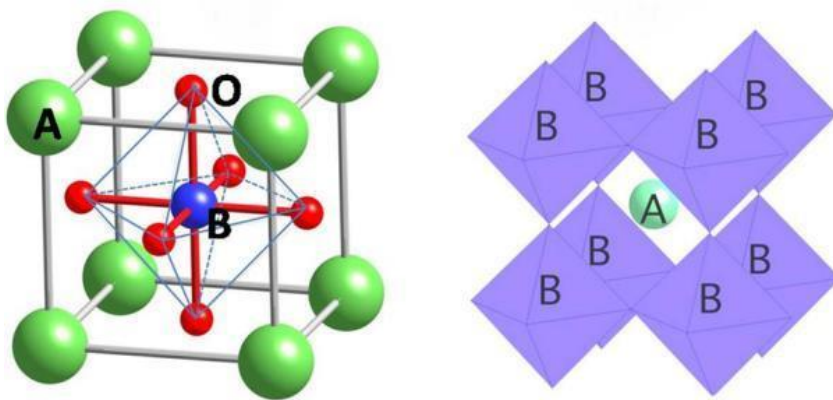


Figure 1.1: Schematic diagram of ABO₃.¹⁵

In the ABO₃ type systems, since the A-site cation (rare earth element (La, Pr, Nd, etc.), or alkaline earth element (Ca, Sr)) is larger than the B-site cation (a transition or p-block element such as Fe, Ti, Al, etc.), B-site cation is hexa-coordinated, forming BO₆ octahedra within the lattice structure,

whereas A-site cation forms polyhedral configuration whose coordination depends on the lattice structure,^{9,16} {(some examples: (a) In the Sr atoms sit in the 12 coordinate A site, while the Ti atoms occupy the 6 coordinate B site.¹⁷ (b) In the LaAlO₃, the La-atoms sit in the 9 coordinate A site, while the Al atoms occupy the 6 coordinate B site.¹⁸

The A-site of majority of the ABO₃ type perovskite structures, which are potential candidates for various applications, are constituted by Rare-earth (RE) cations.¹⁹ The RE-ions are most stable in triply ionized states and the valance $4f^n$ electrons in rare earth ions element are assailed by $5s^25p^6$ outer orbital electrons, and the emission peaks arising in them are generally very sharp and intense since these are less affected by external fields.¹⁹⁻²¹

For this reason, the introduction of RE-ions as dopants in certain systems leads to perturb the unique properties of luminescence.²² Nowadays, researchers are focusing on RE-cation based perovskite systems because of the systematic effect of changes in radii on individual properties of RE-cation. The substitution of R-cation by another RE-ion of smaller radii into an ABO₃ host lattice can build up lattice distortion in the crystal, which can further change structurally sensitive physical properties.⁹ Amid RE-based perovskite systems, RE aluminates (RAIO₃) are one of the well-explored systems and exhibit great potential that has attracted much attention towards the fundamental studies of such systems in terms of structural and optical properties.¹² Many authors have studied the structural, optical, dielectric, and magnetic properties of RAIO₃ in which R = La, Pr, and Nd show the rhombohedral crystal structure with space group (R-3c)^{23,24} ; in contrast, those with R = Gd, Dy, Lu, Eu Tb, Er, and Sm show orthorhombic crystal structure with space group (Pbnm).^{9,25} Here we are focusing on the rhombohedral RAIO₃, by which we want to obtain the signature of crystal field transition.

This signature of crystal field transitions can be observed via optical absorption spectroscopy²⁶ in which the absorption peaks corresponding to crystal field transitions may differ attributing to the bonding schemes of R-

cation and O-anion.⁹ In the case of rhombohedral RAlO_3 , if we are choosing the Nd^{+3} $[[\text{Xe}] 4f^3]$ and $\text{Pr}^{+3}[[\text{Xe}] 4f^2]$, then the crystal field transitions (CFTs) of Nd-ions and Pr-ions will be contributed by the splitting of f-orbitals,^{9,17} But La-ions do not have any unpaired electron in f & d-orbitals.⁹ We know, Crystal field theory describes the breaking of the degeneracy of electron orbital states (f-orbital and d-orbital) due to a static electric field.^{22,27} The changes in static electric field generated by the surrounding charge distribution, specifically the anion neighbors, can be correlated with the changes in bond lengths of corresponding cation-cation or cation-anion pairs.²⁸ This phenomenon is observed in the context of rare-earth ions and ligands. In the crystal lattice, the d-orbitals and f-orbitals of transition metal ions or rare-earth ions experience a splitting into different energy levels due to the electrostatic field.²⁷ Several research groups have discovered crystal field transitions in materials such as garnet and aluminum oxide, particularly when doped with Nd-ions, which exhibit the crystal field splitting effect.²⁹⁻³² This phenomenon has been observed in absorption spectra of Nd-doped $\text{Y}_3\text{Al}_5\text{O}_{12}$ (YAG),³¹⁻³³ $\text{Y}_3\text{Sc}_2\text{Al}_3\text{O}_{12}$ (YSAG),³² $\text{Gd}_3\text{Sc}_2\text{Ga}_3\text{O}_{12}$ (GSGG),³² $\text{La}_3\text{Lu}_2\text{Ga}_3\text{O}_{12}$ (LLGG),³² and Al_2O_3 ,³¹ indicating crystal field transitions. The intensity and energy of these transitions depend on the host lattice and the specific Nd-dopant used.³² For this study, we have chosen NdAlO_3 (NAO) as the parent system, as it inherently exhibits crystal field splitting due to partially filled f-orbitals.⁹ Our aim is to modify the crystal field transitions by introducing a suitable dopant at the Nd site. To achieve this, we have selected La^{3+} as the dopant because it lacks any unpaired electrons in the f-orbital or d-orbital.^{17,24} The presence of La^{3+} will alter the overall environment surrounding the NAO lattice, allowing us to investigate the changes occurring in the crystal field transitions of Nd. These studies may help in fine-tune the energy levels of lasers having Nd as an active medium.

To execute our purpose, we have selected the La-cation as substituent in NdAlO_3 sample to tune the crystal field splitting of Nd-cation for understanding of crystal field splitting of Nd-ions by La-substitution

because La-cation does not show crystal field splitting and these members lie in rhombohedral phase.⁹ These samples have been prepared by sol-gel method and the phase purity of these sample has been confirmed by powder-X-ray diffraction method.³⁴

1.3: Goldschmidt Tolerance factor:

Goldschmidt's tolerance factor is an indicator for the stability and distortion of crystal structures.^{9,35} It is useful to describe the stability in perovskite ABO_3 structure. The Goldschmidt tolerance factor (t) is a dimensionless number that is calculated from the ratio of the ionic radii as shown in **equation (1)** where R_A , R_B , and R_O are the ionic radii of the A-site cation, B-site cation, and oxygen anion, respectively.^{36,35}

$$t = \frac{(R_A + R_O)}{\sqrt{2}(R_B + R_O)} \cong \frac{\langle A - O \rangle}{\sqrt{2} \langle B - O \rangle} \quad (1)$$

Where $\langle A-O \rangle$ and $\langle B-O \rangle$ are bond length.

When R_A decreases, and so 't', the lattice structure transforms to the rhombohedral structure ($t < 0.96$) and then after to orthorhombic structure ($t < 0.92$), in which the Al-O-Al bond angle deviates from 180° .

1.4: Structure of $NdAlO_3$:

Neodymium aluminate is an ABO_3 type perovskite structure.⁹ The rhombohedral $NdAlO_3$ (NAO) does not exhibit any low-temperature structural or magnetic phase transition till ~ 2 K but shows rhombohedral to cubic phase transition at high temperature (~ 1640 K).³⁷ Red photoluminescence in pure NAO has been investigated by Maciel et al.,³⁸ which can be used in phosphor applications as an ultraviolet-to-red converter and in the production of high-power lasers. NAO particles have been used as catalysts for biodiesel synthesis, as reported by Navarrete et al.³⁹ NAO as a solid electrolyte material has been studied by Ishihara et al.⁴⁰ and observed that NAO doped with Calcium and Gallium could be

promising oxide ion conductors. Wide applicability of NAO in different fields and existing crystal field transitions can make it useful in tunable laser or microwave absorbers. Many researchers had been showed that NdAlO₃ are of special interest because luminescence properties of Nd⁺³ ion are promising to develop high power lasers.^{41,42} In the next section, we have discussed the selection of dopants to tune crystal field transitions of Nd-cation.

1.5: Crystal field splitting:

Crystal field transition (CFT) refers to the change in energy that occurs in the electronic configuration of metal ions when they are placed in the crystal field environment.^{27,43} In the crystal field, the transition metal ion of *d*-orbitals and rare-earth ion of *f*-orbitals undergo electrostatic interaction with its surrounding ligands, which can distort the electron cloud and split the energy levels of the *d*-orbitals and *f*-orbitals.²⁸ The crystal field transition involves the excitation/de-excitation of electrons between ground state and higher states corresponding to the degeneracy-lifted orbitals. These transitions can be influenced by various factors such as coordination geometry, ligand identity, absorption of light, or external field.⁴³ A significant amount of research has been carried out to probe the features of CFT in rare earth ions.^{9,20,28} Here, we focus on how the electric field (that lifts the degeneracy of orbitals) changes with metal-ligand bond length. For this purpose, the method of chemical substitution is adopted here. Lanthanum ion (La³⁺) is chosen as a suitable dopant at Nd site, as –

- a) It does not possess any *f-f* transitions, so that slight contribution of modifications in the lattice parameters can occur in the absorption.
- b) The difference in ionic radii between La³⁺ and host Nd³⁺ ions should allow considerable change in the lattice, without introducing any additional defect states due to stoichiometry.

Therefore, by controlling the incorporation of La^{3+} into host NAO lattice, one can tune the crystal field transition. Hence, a brief discussion on CFT in various oxides has been demonstrated in the next section.

1.5.1 Crystal field transitions in various oxides:

Figure 1.2 shows the schematic atomic configuration in which the A-cation and oxygen anions form polyhedral. Considering A-cation as a rare earth element such as $R = \text{Pr}, \text{Nd}, \text{Sm}$, etc. which shows crystal field splitting due to the presence of unpaired f -electrons.^{9,17,44}

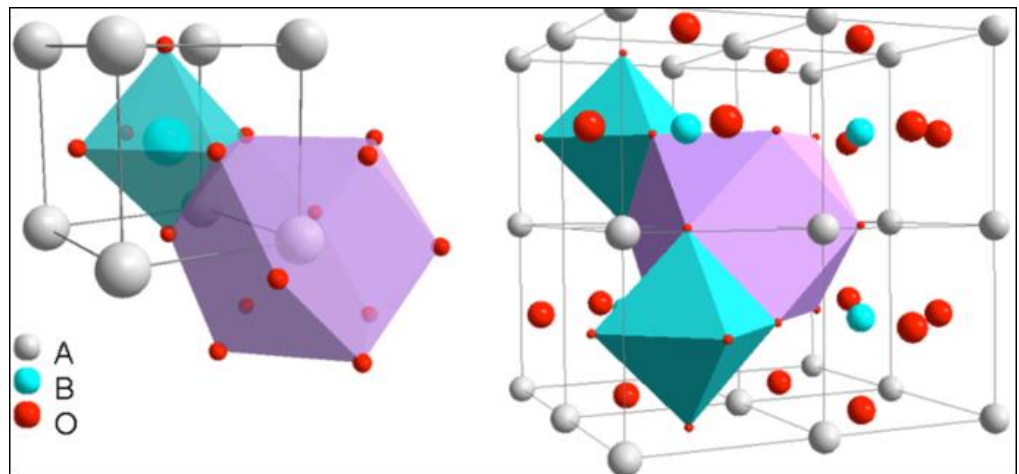


Figure 1.2: ABO_3 type perovskite materials.⁴⁵

In the case of Nd ion, the crystal field transitions (CFTs) will be contributed by the f -orbitals, as shown in schematic **Figure 1.3**. The signature of CFTs can be probed via the optical absorption spectra of the system, where depending upon the system, the absorption peaks corresponding to crystal field transitions may differ, which attributes to the bonding schemes of R-cation and O-anion.^{24,26,46} Looking into the literature, we can see that the absorption spectra correspond to crystal field transitions of the Nd-doped yttrium aluminum garnet^{46,47} and aluminum oxide³¹ system as shown in **Figure 1.4** (upper and lower images, respectively).

Our interest is to explore the effects of such splitting in f -orbital systems.

$\text{Nd}^{3+}:\text{YAG}^{46}$ and crystal-field terms that split each multiple $4f^3, 2s+1L_J$ into $J_{+1/2}$ energy level as shown in **Figure 1.3**

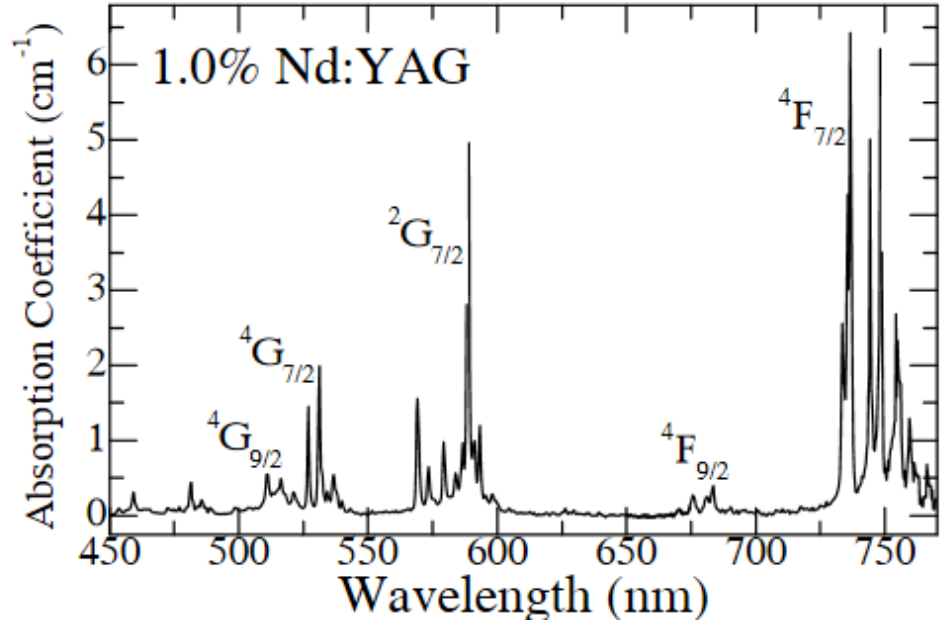


Figure 1.4: Optical absorption spectra of Nd-doped Yttrium Aluminate Garnet.⁴⁶

Now, from **figure 1.4**, addition of Nd in this system shows the signature of crystal field transitions in optical absorption spectra. The intensity and energy of these transitions would depend on the host lattice as well as Nd-dopant. As far as literature is concerned, we have selected ABO_3 type-perovskite NdAlO_3 as a parent system where the crystal field splitting occurs intrinsically and attempt to tune the transitions by suitable dopant at Nd site.

1.6 Selection of Dopant:

To achieve this, we have selected La^{3+} as the dopant ion. La^{3+} does not possess any unpaired electrons in its f-orbital and do not show any crystal field transition, hence which allows it to modify the overall surrounding

environment of the Nd ions in the NdAlO₃ lattice due to difference in the ionic radii of Nd³⁺ (1.163) and La³⁺ (1.216) ions. By incorporating La³⁺ dopant, we can investigate and observe the resulting changes in the crystal field transition of Nd ions. This dopant selection enables us to tune the crystal field splitting of Nd³⁺, making it a potentially useful lasing center. By studying the effects of La³⁺ doping on the crystal field transitions in NdAlO₃, we aim to gain insights into the fundamental principles governing these transitions and pave the way for potential applications in laser technology and other optoelectronic devices.

Chapter 2

Experimental Section:

In this chapter, we provide an overview of the experimental techniques employed in this study. The Sol-gel synthesis method was utilized for sample preparation, allowing us to obtain the desired polycrystalline samples. We discuss the key steps involved in the Sol-gel synthesis process and highlight its advantages for our research purposes.

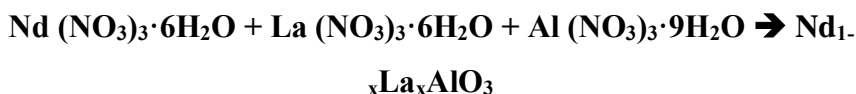
Furthermore, we delve into the characterization techniques employed in this work, including X-ray diffraction (XRD), Raman spectroscopy, and optical absorption spectroscopy. XRD analysis enables us to determine the structural properties of the synthesized samples and confirm the presence of the desired rhombohedral phase. Raman spectroscopy provides valuable insights into the vibrational modes and crystal symmetry of the materials under investigation. Lastly, optical absorption spectroscopy allows us to probe the crystal field transitions and obtain information about the energy levels and intensity of these transitions.

Here, we discuss an overview of the experimental techniques used in the present work. In this chapter, description on the Sol-gel synthesis method used for sample preparation, important characterization tools such as XRD, Raman Spectroscopy, and optical absorption spectroscopy have been presented.

2.1 Sample synthesis via Sol-gel method

The Sol-gel⁵⁰ process is a wet chemical method for the synthesis of various metal oxide nanoparticles. In this method, a molecular precursor is dissolved in distilled water, and it is converted to gel by heating, undergoing hydrolysis process. Since then, some processes have been involved in sol-gel synthesis, such as Condensation, Ageing, Drying, and Calcination.⁵⁰ Thus, the overall process we have used for the synthesis of Nd_{1-x}La_xAlO₃ is discussed below.

The Sol-gel method has been used for the preparation of compositions of La-substituted NdAlO₃ samples. For the preparation of Nd_{1-x}La_xAlO₃ compositions (x = 0, 0.1, 0.2, 0.3, 0.4, 0.5), stoichiometric proportions of metal nitrates, citric acid, and ethylene glycols have been measured according to the following reaction²⁴ –



The aqueous solutions for the precursors of NdAlO₃ and La-substituted NdAlO₃ as final products were prepared by dissolving stoichiometric amounts of Neodymium (III) nitrate hexahydrate Nd (NO₃)₃·6H₂O (purity 99%, Sisco Research Laboratories), lanthanum (III) nitrate hexahydrate La (NO₃)₃·6H₂O (purity 99%, Sisco Research Laboratories) and aluminum (III) nitrate Nona-anhydrate Al (NO₃)₃·9H₂O (purity 98.00%, Loba) in distilled water, with continuous stirring at 373 K temperature. After that, Citric acid (purity 99.5%, Loba) and ethylene glycol (purity 99%, Loba) were added to the transparent solution as a catalyst and gelation agent, respectively. The resulting solution was heated and stirred for about 50 minutes, until the gel formed and for further heat treatment, the gel containing vessel was put in a muffle furnace for 10 hours at 573K temperature, till the dry gel formed. After this, grinding of the Gel dry was done and followed by further heat treatments for calcination in the muffle furnace for 12 hours at temperatures ~ 623K and ~ 973K with intermediate

grinding.⁹ The product has been obtained in homogeneous dry powdered form for which all characterizations have been performed.

Table2.1: Nomenclature of Composition.

Sr. No.	Sample series (Rare earth aluminate)	Stoichiometric formula	Chemical Composition
1.	La-Substituted NdAlO₃	Nd_{1-x}La_xAlO₃	NdAlO₃
2.			Nd_{0.9}La_{0.1}AlO₃
3.			Nd_{0.8}La_{0.2}AlO₃
4.			Nd_{0.7}La_{0.3}AlO₃
5.			Nd_{0.6}La_{0.4}AlO₃
6.			Nd_{0.5}La_{0.5}AlO₃

2.2 X-ray Diffraction:

X-ray diffraction (XRD) studies are widely used for determining the structural characterization of unknown solid materials in geology, environmental science, materials science, engineering, and biology.⁵¹⁻⁵³

XRD is a non-destructive technique for understanding how atoms are arranged and how such arrangements can affect the behavior of materials and it can be used to determine the structure of complex molecules, crystallite size, lattice parameter, lattice strain, phase identification, and inter planer distance between two planes of sample.^{24,54} The experimental technique utilizes the phenomena of diffraction of X-rays for determining the atomic arrangements in the system because the atomic spacing resembles with wavelength of X- rays, satisfying the necessary condition of diffraction of wave.

X-rays are electromagnetic radiation of extremely short wavelength and high frequency, with wavelengths ranging from about 10^{-8} to 10^{-12} meter and corresponding frequencies from about 10^{16} to 10^{20} hertz (Hz) and lie between gamma rays and ultraviolet radiation in the electromagnetic spectrum.⁵² X-rays have energy in the range of 200eV to 1MeV. X-rays are produced by accelerating charged particles, the external beam of electrons interacts with electrons in the shell of an atom. X-rays are generated in a cathode ray tube by heating a filament to produce electrons, accelerating the electrons toward a target by applying a voltage, and bombarding the target material with electrons. When electrons have sufficient energy to dislodge the inner shell electrons of the target material then a hole is left in the inner shell. When this hole is fitted by an outer shell electron, characteristic X-ray spectra are produced.⁵³ This spectrum consists of several components, with the most common being K_{α} and K_{β} . K_{α} consists, in part, of $K_{\alpha 1}$ and $K_{\alpha 2}$. $K_{\alpha 1}$ has a slightly shorter wavelength and twice the intensity as $K_{\alpha 2}$. The emitted wavelengths are characteristics of the target material (Cu, Fe, Mo, Cr). Copper is the most common target material for single-crystal diffraction, with Cu K_{α} radiation = 1.5418\AA .⁵³

2.2.1 Principle:

In XRD, an X-ray falls on the sample at an incident angle θ and gets diffracted through a different set of atomic planes in the crystal structure of

the sample. The basic principle of XRD can be understood with the help of a schematic ray diagram.

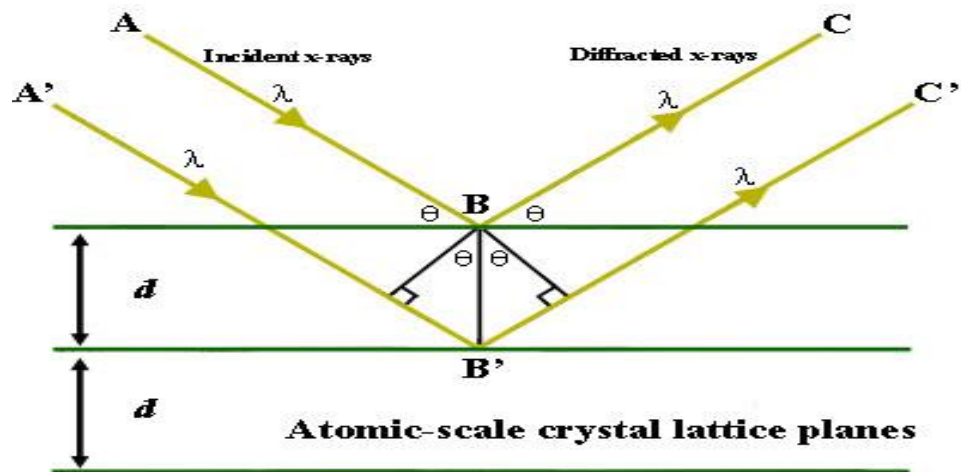


Figure 2.1: Diffraction of X-ray by a crystal.⁵⁵

According to the figure, the path difference between ABC and A'B'C'.

Path difference (Δ) = B'N'+BN

$$\Delta = BB' \sin\theta + BB' \sin\theta \quad (2.1)$$

$$\Delta = 2BB' \sin\theta \quad (2.2)$$

In this figure, where BB' is equal to 'd', here 'd' is interplanar distance.

Now, in the above equation, we can write.

$$\Delta = 2d \sin\theta \quad (2.3)$$

For constructive interference, the path difference is an integer multiple of the wavelength.

i.e.,

$$\Delta = n\lambda \quad (2.4)$$

Where n is an integer.

Thus, from the equations (2.3) and (2.4), we obtained -

$$2d\sin\theta = n\lambda \quad (2.5)$$

This is Bragg's condition for constructive interference of diffracted X-rays.

(here, λ is the wavelength of the incident X-ray, d is the interplanar distance, θ is the incident angle of the X-ray, and n is an integer.

The spacing of the atoms in the crystal lattice is in the same order as the wavelength of the X-rays (0.01 to 100 Å).

2.2.2 X-ray diffractometer:

X-ray diffractometer consists of several main components:

1. X-ray Source
2. Sample stage
3. X-ray Detector

The parameters during the diffraction have been as follows: Tube current-40mA, Tube voltage-40kV, Range of scan-20 to 84° (2θ), Wavelength used-1.5406Å (Cu $K\alpha$), step size-0.02 degree and scanning speed of 0.5 degree/minute.

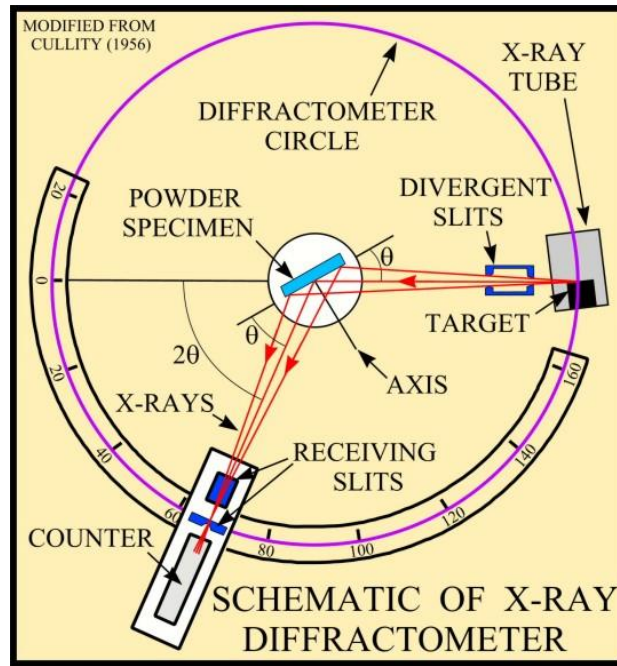


Figure 2.2: Schematic diagram of X-ray Diffractometer.⁵⁶

X-ray diffractometer can be arranged into two ways- first $\theta:\theta$ arrangement in which sample is fixed and X-ray source and detector rotates with angle θ° per minute and other one is $\theta:2\theta$ arrangement in which X-ray source is fixed; Sample rotates with angular speed θ° per minute while x-ray detector rotates with angle $2\theta^\circ$ per minute with respect to the beam source.^{34,56}

2.2.3 Working:

The monochromatic X-ray falls on the surface of sample, “bouncing” off the atoms in the structure and changing the direction of the beam at some different angle, theta, from the original beam. This is the angle of diffraction. When the geometry of the incident X-rays affecting the sample satisfies the Bragg equation, constructive interference occurred and a peak in intensity occurs. A detector processes this X -ray signal than output is recorded by computer device.

Intensity of diffracted X-ray depends on the density of electrons in different planes and on the orientation of the planes of the crystal. Intensity of diffracted X-rays can be calculated by using structure factor F. Structure factor written as:⁴³

$$F = f_j[-2\pi i(hx_j + ky_j + lz_j)] \quad (2.6)$$

Where f_j is the atomic scattering factor and h, k and l are the miller indices of the reflection. The position of the atoms in unit cell are x_j, y_j, z_j .

The intensity is:

$$I = |F|^2 = F * F^* \quad (2.7)$$

Reflection for which $|F|^2 = 0$ will have zero intensity and there is no diffraction pattern (forbidden reflections).⁴³

2.3 Diffuse Reflectance spectroscopy (DRS):

UV visible spectroscopy is an optical spectroscopy technique in which we study the light absorbed in UV and visible region of electromagnetic spectra. The range of wavelength in UV and Visible regions of electromagnetic spectra are 200nm to 800nm. DRS is based on the diffused reflection, in which when light is fall on the surface of powder sample, it gives two types of reflection, one is non-specular (diffuse reflection) and other is specula reflection as shown in **Figure-2.3**.

Specular reflection: - Specular reflection reflects all light which arrives from a given direction at the same angle. i.e., Specular reflection, in which incident angle equal to reflected angle.

Diffuse reflection: - Diffuse reflection is the reflection of light from a surface of powder where incident ray is reflected at many angles. i.e., incident angle not equal to reflected angle.

For reflecting surface, the reflectance (for normal incidence) can be written in term of refractive index, i.e.,

$$R = \frac{(n - 1)^2}{(n + 1)^2} \quad (2.8)$$

Here, R is reflectance and it's used to measure the smooth surface of sample. But this formula is not valid for rough surface of sample, which is usually the case in physical samples. So, for this problem to be resolved, the DRS has been used. In DRS, the detector is measured to reflectance according to Kubelka Munk function.⁵⁷

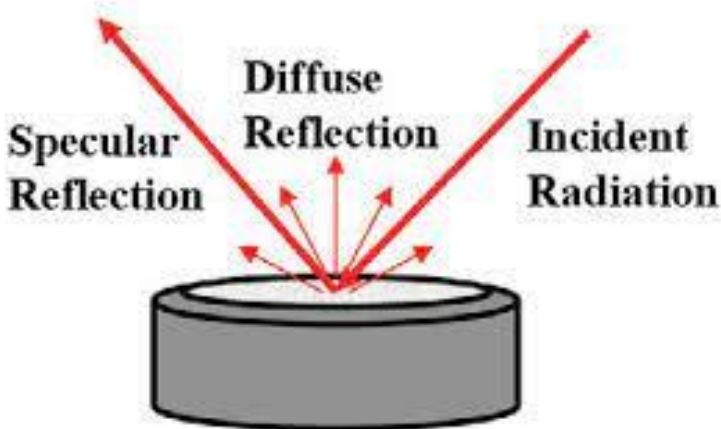
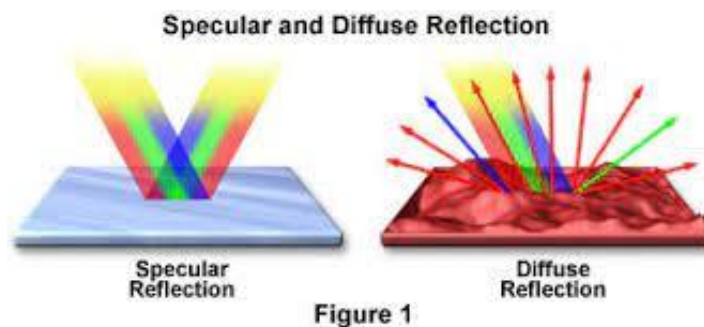


Figure 2.3: Schematic diagram of Specular and Diffuse Reflection.⁵⁸

2.3.1 Principle of DRS:

When the UV-Visible light falls on the surface of powder sample, it is reflected in all directions due to roughness of the surface of powder (sample). Some light goes inside the sample under multiple scattering and fraction of emitted back into the detector. Some light may be a specular reflection from the surface of powder. Some part of electromagnetic wave may also undergo transmission and enters the powder, and it is reflected from small grain of powder sample, but probability of transmitted light is gone from powder sample become zero. So here incident light either gets absorbed or reflected, but here transmission light is negligible.

DRS can be used to find the bandgap, crystal field transition, refractive index, thickness of the thin film, the signature of Urbach energy, and temperature-dependent band gap.^{54,59}

To estimate the optical band gap, the diffuse reflectance spectra have been converted to equivalent absorption spectra using Kubelka-Munk Function.⁵⁷

According to the Kubelka-Munk model, the radiation field is approximated by two fluxes, one, I , traveling from the illuminated sample surface, and the other, J , traveling toward the illuminated surface. As light travels from the surface of a sample, its intensity decreases due to scattering and absorption processes, his model is based on the following differential equations.

The component travelling from the illuminated surface:

$$dI = -KIdx - SIdx + SJdx \quad (2.9)$$

The component travelling toward the illuminated surface:

$$dJ = -KJdx - SJdx + SIdx \quad (2.10)$$

Where, I and J are the intensities of light traveling inside the sample towards its illuminated and un-illuminated surface (from its illuminated),

respectively; dx is the differential segment along the light path; S and K are the Kubelka-Munk scattering and absorption coefficients, respectively.

let's

$$\alpha = \frac{(S + K)}{S} \quad (2.11)$$

We can write,

$$\frac{-dI}{Sdx} = -\alpha I + J \quad (2.12A)$$

$$\frac{-dJ}{Sdx} = -\alpha J + I \quad (2.12B)$$

Combining into a single differential equation,

$$\frac{dR}{Sdx} = R^2 - 2\alpha R + 1 \quad (2.13)$$

Where $R=J/I$.

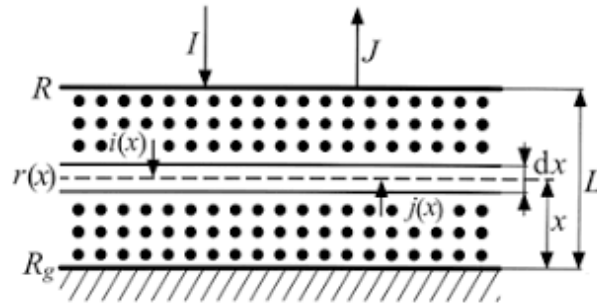


Figure 2.4: Schematic diagram for the Kubelka-Munk analysis of reflectance and transmittance of a scattering medium.⁵⁷

If the equation is integrated over the limits $x=0$ to $x= \infty$, we can obtain a simple formula

$$R_{\infty} = \alpha - (\alpha^2 - 1)^{0.5} \quad (2.14)$$

and now, rearranged to give the well-known Kubelka-Munk function $F(R_\infty)$

$$F(R_\infty) = \frac{K}{S} = \frac{(1 - R_\infty)^2}{2R_\infty} \quad \#(2.15)$$

The Kubelka-Munk function is based on some assumptions.

1. No external or internal surface reflections occur.
2. The medium is considered homogeneous and isotropic.
3. The only interaction of light with medium is absorption and scattering; polarization and spontaneity are ignored.
4. The sample is modeled as a plane layer of finite thickness.

In the limiting case of an infinitely thick sample, the K-M equation at any wavelength becomes:

$$F(R_\infty) = \frac{K}{S} = \frac{(1 - R_\infty)^2}{2R_\infty} \quad (2.17)$$

$R_\infty = \frac{R(\text{Sample})}{R(\text{standard})}$. $R(\text{Sample})$ is the diffuse reflectance of the sample and

$R(\text{Standard})$ is that of the standard.

The Kubelka-Munk function is directly proportional to the absorption coefficient (α);

$$F(R_\infty) \propto \alpha \propto \frac{(h\nu - E_g)^{\frac{1}{n}}}{h\nu} \quad (2.18)$$

Where $n = 1$ for direct band gap, and $n = \frac{1}{2}$ for indirect band gap

2.3.2 Instrument:

The UV-Visible Spectrometer is an analytical instrument that employs light scattering from the sample to observe the electronics modes in molecules.

UV-Visible Spectrometer consists of several main components:

1. Light Source

2. Integrating Sphere
3. Monochromators
4. Sample
5. Detector
6. Computer

The instrument of UV-Visible Spectrometer is shown as:



Figure 2.5: Experimental set up utilized for diffuse reflectance measurement, (a) Carry 60 UV-Visible Spectrometer, (b) Internal set up of UV-Visible spectrometer.⁶⁰

2.3.3 Working:

A diffuse reflectance has been measured by an attachment to a UV-Visible spectrometer. Xenon lamp is used for producing the UV-Visible spectrum, this spectrum passes through various filters and monochromator and after

doing some optical arrangement, finally light is incident on the sample and diffused reflected light is detected by the detector.

2.4 Raman Spectroscopy:

The Raman effect, which forms the basis of Raman spectroscopy, was discovered by the Indian physicist Sir C.V. Raman in 1928.⁶¹ Raman spectroscopy is a powerful analytical technique used to study the vibrational modes of molecules and materials.^{24,62–64,64} It is based on the inelastic scattering of light, where a small fraction of incident photons undergoes a change in energy due to interactions with molecular vibrations, resulting in the emission of scattered photons with a different energy and wavelength.⁶³ Raman spectroscopy can provide information about the molecular structure, chemical composition, and crystalline properties of a sample. It is a non-destructive technique, and it can be used for the analysis of solids, liquids, and gases. The change in the polarizability of the molecule can be related to the change in the dipole moment of the molecule during the vibrational transition. The dipole moment is equal to that of the product of the polarizability of molecule and the electric field of the incident light source and can be expressed as:⁶¹

$$P = \alpha E_0 \cos(2\pi f_0 t) \quad (2.4.1)$$

Where, E_0 is the intensity, α is the polarizability and f_0 is the frequency of the electric field of the incident light. If the molecule is vibrating with a frequency f_m , the nuclear displacement q is written as:

$$q = q_0 \cos(2\pi f_m t) \quad (2.4.2)$$

Where, q_0 is the vibrational amplitude.

If α is the linear function of q then from Taylor series expansion:

$$\alpha = \alpha_0 + \left(\frac{\partial\alpha}{\partial q}\right) \alpha_0 + \dots, \quad (2.4.3)$$

From eq. (2.4.1), (2.4.2) and (2.4.3).

$$\begin{aligned} P = & \alpha E_0 \cos(2\pi f_0 t) \\ & + \frac{1}{2} \left(\frac{\partial\alpha}{\partial q}\right) q_0 E_0 [\cos(2\pi(f_0 - f_m)t) \\ & + \cos(2\pi(f_0 + f_m)t)], \end{aligned} \quad (2.4.4)$$

According to classical theory of Raman scattering, the first term represents as Rayleigh scattering, while second term represents Raman scattering due to Stokes ($f_0 - f_m$) and anti-Stokes ($f_0 + f_m$) term. **Figure 2.6** shows the schematics of Raman scattering.

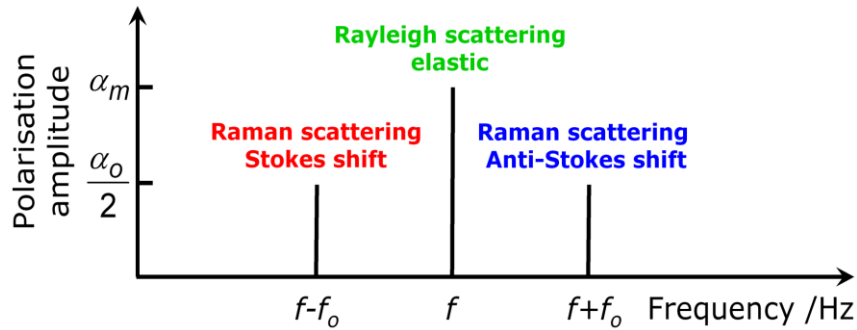


Figure 2.6: Schematic representation of Raman Scattering.⁶⁵

2.4.1 Raman Spectrometer:

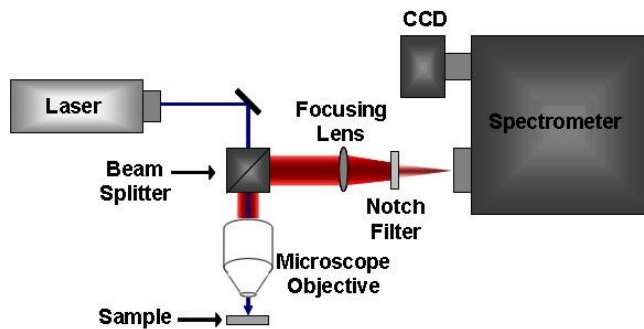


Figure 2.7: Raman Spectrometer from ref.⁶⁵

A Raman spectrometer is an analytical instrument that employs light scattering from the sample to observe the vibrational modes of molecules.

A Raman Spectrometer consists of several main components:

1. Laser
2. Sample
3. Focusing Mirror
4. Monochromator
5. Detector
6. A recording device/ computer.

Chapter-3

Results and Discussion:

3.1 Structural characterization using X-ray diffraction:

The X-ray diffraction (XRD) method was used to verify the phase purity of pure and La-substituted NdAlO_3 samples, as shown in **Figure 3.1**. The XRD peaks of both the pure and La-substituted samples matched well with each other, indicating no impurity peaks were observed. The Rietveld refinement technique⁶⁶ was employed, considering the R-3c space group (167), to analyze the Pure and La-substituted NdAlO_3 samples.^{9,24,59} **Figure 3.1 (b)** presents a schematic representation of the Rietveld refined data for the 20% La-substituted sample ($\text{Nd}_{0.8}\text{La}_{0.2}\text{AlO}_3$). The absence of impurity peaks was confirmed in the XRD data.³⁴

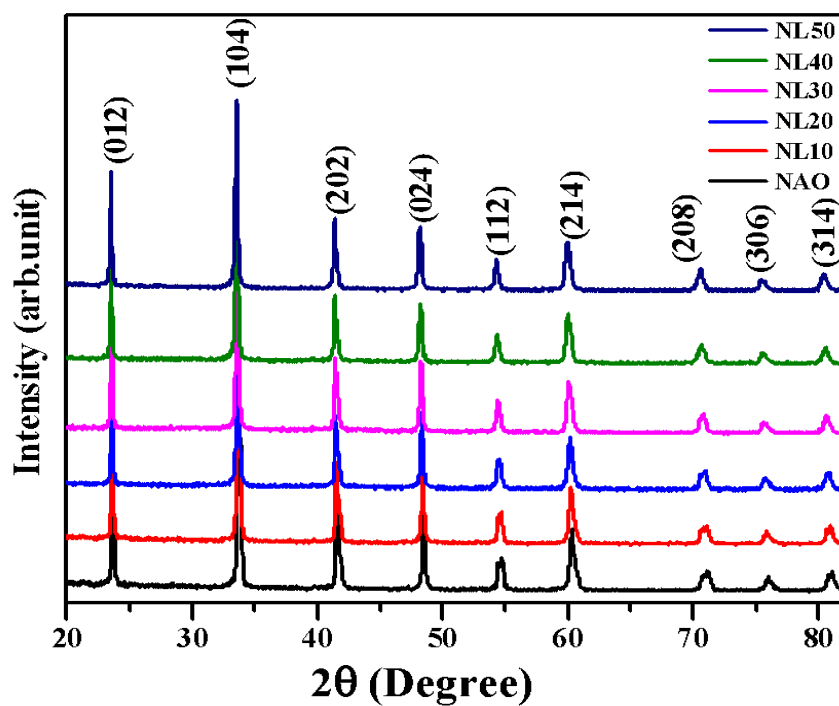
Furthermore, a systematic decrease in the 2θ positions of the peaks was observed in **Figure 3.2 (a)**, indicating an increase in the lattice parameters a and c after La-substitution due to the larger size of La. The increase in lattice parameters was also confirmed through Rietveld refinement,⁶⁶ as depicted in **Figure 3.2 (b)**. The crystallographic information, including lattice parameters, bond lengths, and bond angles, was extracted using VESTA software.⁶⁷ The values of these parameters are tabulated in **Table 3.1**. Overall, the lattice parameters, bond lengths (Nd/La-O), and cell volume systematically increased with La content.

Additionally, the Al-O distances in AlO_6 octahedra were observed using VESTA software⁶⁷ for different La concentrations. It was observed that out of the nine Nd/La-O bond lengths, three Nd/La-O₁ bond lengths formed a triangle in the out-of-plane direction, while the other six in-plane Nd/La-O₂ bond lengths had equal values. These bond length values are presented in **Table 3.1** for all the samples.

Table 3.1: Crystallographic information extracted from Rietveld refinement method with space group R-3c:

Name		NAO	NL-10%	NL-20%	NL-30%	NL-40%	NL-50%	
Lattice Parameter	a=b (Å)	5.315(1)	5.320(1)	5.325(1)	5.330(1)	5.335(2)	5.339(2)	
	c (Å)	12.926(6)	12.944(6)	12.964(6)	12.984(7)	13.005(8)	13.025(8)	
	$\alpha = \beta, \gamma$	90°, 120°	90°, 120°	90°, 120°	90°, 120°	90°, 120°	90°, 120°	
Cell Volume	V (Å ³)	316.364	317.314	318.428	319.451	320.611	321.633	
Wyckoff Positions	Nd/La	X	0	0	0	0	0	
		Y	0	0	0	0	0	
		Z	0.25	0.25	0.25	0.25	0.25	
	Al	X	0	0	0	0	0	
		Y	0	0	0	0	0	
		Z	0	0	0	0	0	
	O	X	0.5449	0.5447	0.5408	0.5375	0.5379	
		Y	0	0	0	0	0	
		Z	0.25	0.25	0.25	0.25	0.25	
	Bond Angle (°)	Al-O-Al	165.5(5)	165.5(5)	166.8(6)	167.9(7)	167.7(7)	167.8(6)

	Nd/La-O-Nd/La	169.7 (4)	169.7 (4)	170.6 (4)	171.4 (5)	171.3 (5)	171.4 (4)
Octahedral tilt ϕ		8.840	8.802	8.044	7.41	7.47	7.44
Bond length (\AA)	Al-O	1.8901 (11)	1.8918 (10)	1.8915 (11)	1.8916 (11)	1.8941 (12)	1.8960 (10)
	Nd-O₁	2.419 (9)	2.422 (9)	2.446 (10)	2.465 (11)	2.465 (11)	2.469 (9)
	Nd-O₂	2.6559 (8)	2.6589 (7)	2.6607 (8)	2.6628 (8)	2.6667 (9)	2.6701 (7)



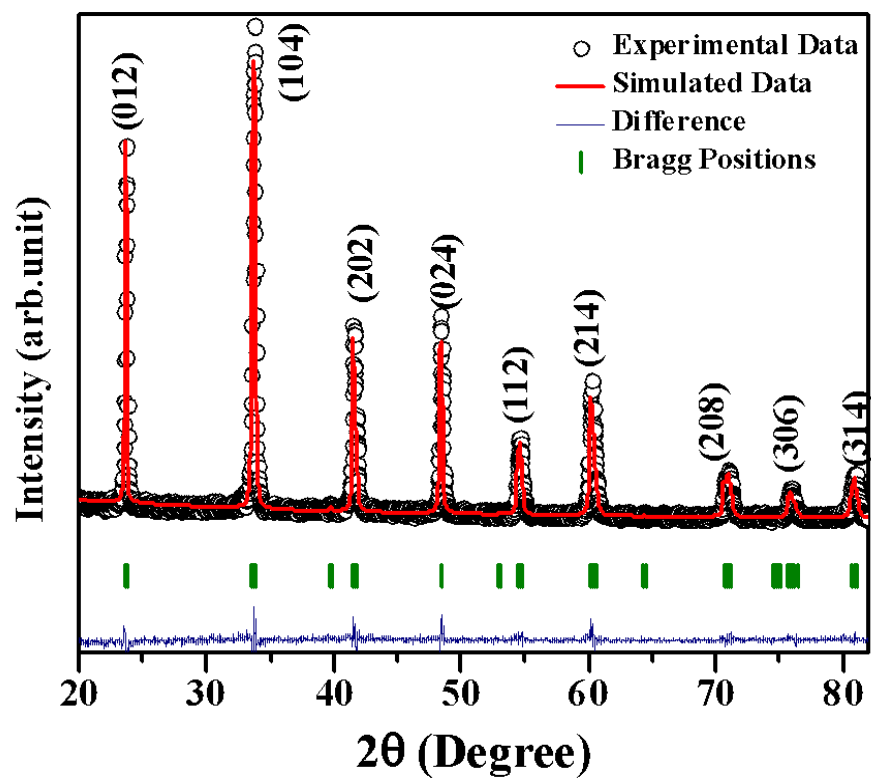


Figure 3.1: (a): X-ray diffraction data of pure and La-substituted NAO system. (b): Rietveld refinement pattern for La; NAO using space group R-3c.

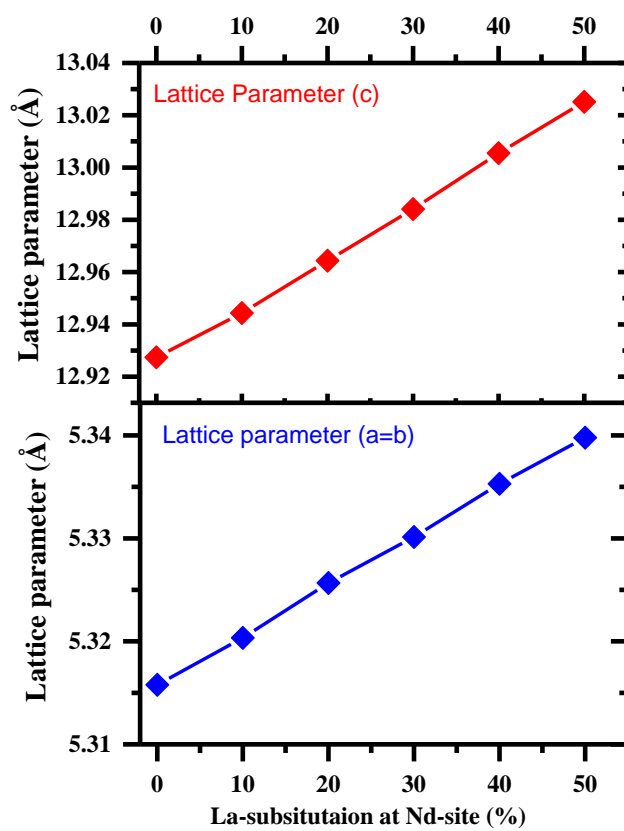
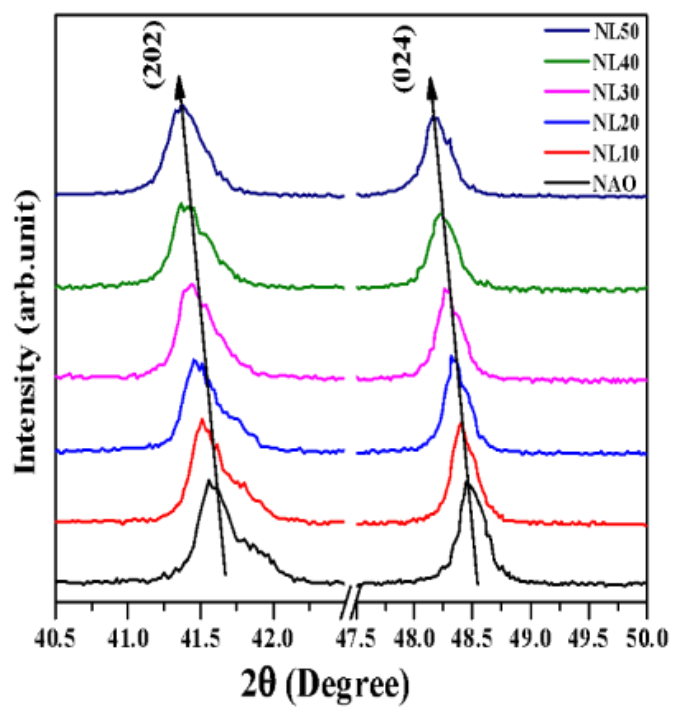


Figure 3.2: (a): Magnified view of X Ray-Diffraction of La-substituted NdAlO₃. (b): Variation of Lattice parameter.

The equation of tolerance factor:

$$t = \frac{\left(\frac{R_{Nd}}{La} + R_O\right)}{\sqrt{2}(R_{Al} + R_O)} \cong \frac{\langle Nd - O \rangle}{\sqrt{2} \langle Al - O \rangle} \quad (3.1)$$

Where average bond length of $\langle Nd - O \rangle = \left(\frac{[(Nd-O1)+(Nd-O2)]}{2}\right)$, the value of these bond lengths has been given in the table (3.1).

The tolerance factor has been used to describe stability in the Nd_{1-x}La_xAlO₃ sample using the equation (3.1), where R_{Nd} (1.163Å), R_{La} (1.216Å), and R_O (1.38Å) represent the ionic radii of Nd-cation, La-cation, Al-cation, and O-anion, respectively. The obtained value of t is increasing, when ionic radii of La-cation on the Nd side are increased. The increasing value of t, which suggests a decrease in the lattice distortion. The rhombohedral (R-3c) structures show a $\bar{a}\bar{a}\bar{a}$ tilt rotation in AlO₆ octahedra according to the Glazer notation. The rhombohedral distortion is result of the rotation of O-anion octahedra in the R-3c perovskite material. The value of t in Nd_{1-x}La_xAlO₃ sample is 0.9492(x=0), 0.9495(x=0.1), 0.9545(x=0.2), 0.9584(x=0.3), 0.9578(x=0.4), and 0.9583(x=0.5).

The angle of rotation of octahedra is given by as:²⁴

$$\tan(\varphi) = 2\sqrt{3}\left(x(o) - \frac{1}{2}\right) \quad (3.2)$$

$$\varphi = \tan^{-1}\left(2\sqrt{3}\left(x(o) - \frac{1}{2}\right)\right) \quad (3.3)$$

The relation of octahedral rotation angle has been taken from a literature survey. For calculating octahedral rotation angle in rhombohedral structures in which the Wyckoff-position X(O) and lattice parameter have been observed from Vesta-Software. The value of octahedral rotation angle (φ) has been given in table 3.1.

In the $\text{Nd}_{1-x}\text{La}_x\text{AlO}_3$ samples, as the concentration of La increases on the Nd site, the octahedral tilt angle is observed to decrease. This decrease in the tilt angle indicates less distortion in the lattice structure. The structural distortion associated with the AlO_6 octahedra is analyzed by examining the bond angles involving the Nd/La-O-Nd/La and Al-O-Al interactions. It has been observed that changing the Wyckoff position of the oxygen atom X(O) also affects the distortion of the AlO_6 octahedra.

3.2 Optical absorption spectroscopy:

Figure 3.3 depicts the optical absorption spectroscopy in diffuse reflectance mode⁵⁷ of as-prepared $\text{Nd}_{1-x}\text{La}_x\text{AlO}_3$ powder within the range of 200-900 nm. In diffuse reflectance mode,⁵⁷ the function $F(R)$ is related to reflectance R , and the Kubelka-Munk function is used to analyze the data. In diffused reflectance mode for powder samples, it has been presumed that the reflected light scatters in a perfectly diffuse manner and the scattering function (S) is nearly constant with wavelength. The Kubelka-Munk function is:

$$F(R) = \frac{K}{S} \quad (3.4)$$

where K and S represent the Kubelka-Munk absorption and scattering functions, respectively.^{57,38}

In diffuse reflectance mode, the Kubelka-Munk function is proportional to the absorption coefficient (α).²⁴

$$F(R) \propto \alpha \quad (3.5)$$

According to Tauc's equation

$$(\alpha h\nu)^n = A(h\nu - E_g) \quad (3.6)$$

From equation (3.5) and (3.6)

$$F(R) \propto \frac{(h\nu - E_g)^{\frac{1}{n}}}{h\nu} \quad (3.7)$$

Where n has the value of 2, 0.5 for direct and indirect bandgap transition, respectively.

The allowed optical bandgap transition in $\text{Nd}_{1-x}\text{La}_x\text{AlO}_3$ is from 2p level of Oxygen to (4f, 5d) level of Nd/La within the energy range 0–6.80 eV.

The band edge absorption of the as-prepared $\text{Nd}_{1-x}\text{La}_x\text{AlO}_3$ sample has been observed at 300nm, where $x = 0, 0.1, 0.2, 0.3, 0.4, 0.5$.

Herein, systematic decrement in the optical bandgap with increasing ionic radii La-cation in Nd-site can be understood in terms of increment in Al–O bond length. An increment in Al–O bond lengths increase the interatomic distance with increasing radii of La-cation in Nd-site. In the case of smaller bond lengths, the electrons are firmly bound to each other and stay in a valence band. Thus, with increasing Al–O bond length, the energy 5.37 ± 0.1 is required to excite an electron from the valence to conduction band, and hence, the energy bandgap decreases with increasing ionic radii of La-cation in Nd-site.

The optical bandgap of NAO materials has been calculated as shown in inset Fig. 3.5, and the obtained band gap values are 5.37 ± 0.1 , respectively.

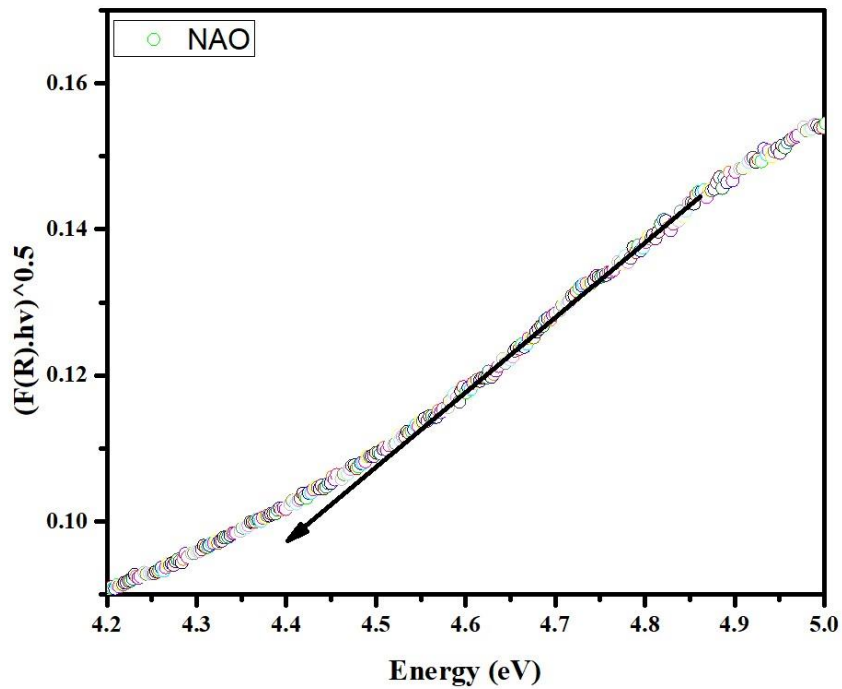


Figure 3.5: The Tauc plot for bandgap calculations.

In **Figure 3.3**, the optical absorption data of La-substituted NdAlO₃ samples are shown, and it can be observed that the crystal field transitions from the ⁴I_{9/2} state to different states (7-crystal field transitions) are present.²⁴ Up to 50% La substitution, all the crystal field transitions are evident. It is interesting to investigate how La substitution affects the crystal field transitions of the Nd cation.

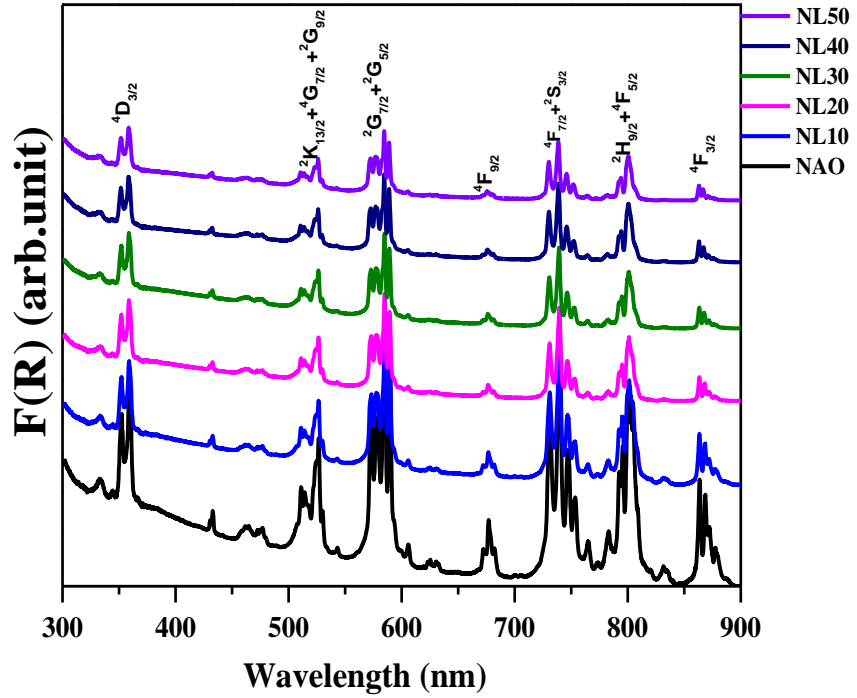


Figure 3.3: Optical absorption spectra of La-substituted NdAlO₃ showing crystal field transitions.

The color of lanthanide ions or rare earth synthesized materials is identified by crystal field transitions. In Nd_{1-x}La_xAlO₃, where La is in the +3-oxidation state with an electronic configuration of La³⁺(Xe, 4f⁰ 5d⁰), there are no f electrons or the possibility of d-d transitions. As a result, La³⁺ does not exhibit crystal field transitions and appears white.

On the other hand, Al is in the +3-oxidation state with an electronic configuration of Al³⁺(Ne, 3s⁰ 3p⁰), and Nd is in the +3-oxidation state with an electronic configuration of Nd³⁺(Xe, 4f³ 5d⁰). This configuration allows for f-f transitions. The absorption transitions in the wavelength range of 200-900 nm correspond to these f-f transitions.

These crystal field transitions exhibit a shift towards lower wavelengths, as shown in **Figure 3.4**. This shift can be correlated with the Nd/La-O bond length, which is related to the electrostatic energy. As the

Nd/La-O bond length and the overall volume of the Nd/La site change, the electrostatic energy and the entire crystal field splitting are modified.

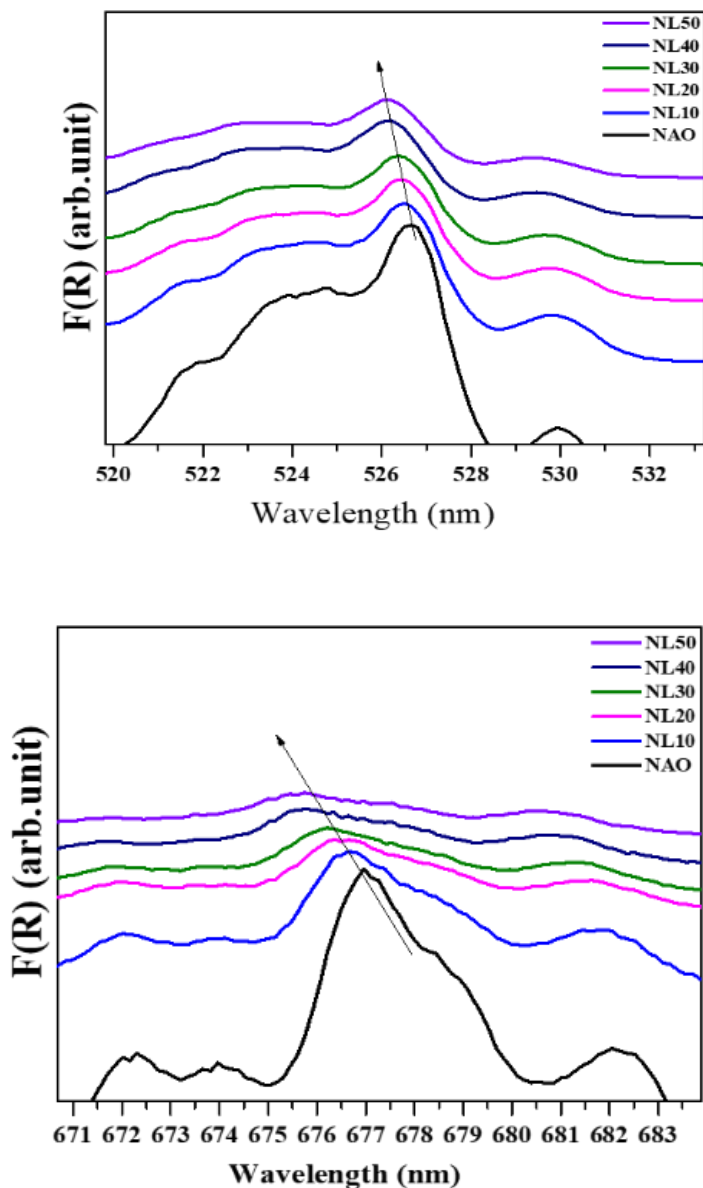


Figure 3.4: Magnified view of crystal field transitions that are tuned by the La-incorporation in the NdAlO₃ host-lattice.

Here, we'll discuss the correlation between bond length and the potential energy difference between two nearby absorption peaks (i.e., the energy difference is calculated by considering the difference between two peaks corresponding to the same member of the series as shown below in **Figure**

3.5). The values of energy corresponding to these peaks are tabulated in the table.

Table 3.2: Variation of transition energy and bond length.

$\text{Nd}_{1-x}\text{La}_x\text{AlO}_3$	Bond length(Å)	Energy (E_1) (eV)	Energy (E_2) (eV)	Energy Difference (meV)
La-0%	2.6559(8)	1.4276	1.4358	8.2
La-10%	2.6589(7)	1.4281	1.4361	8.0
La-20%	2.6607(8)	1.4284	1.4361	7.7
La-30%	2.6628(8)	1.4291	1.4363	7.2
La-40%	2.6667(9)	1.4301	1.4368	6.7
La-50%	2.6701(7)	1.4309	1.4369	6.0

In **Figure 3.6**, the potential energy difference is decreasing as the bond length (Nd-O₂) is increasing. The correlation of bond length and crystal field transition may be realized as the orbital overlapping between the Nd and O ions is observed to vary with La substitution as evident from the bond length value. Due to this altered overlapping, the energy difference between crystal field splitting levels may also get affected which is seen as the decrease in the difference energy value (**Figure 3.6**).

Thus, it can be inferred that the increase in the bond length weakens the crystal field splitting which is experimentally observed as a weakening of the intensity of crystal field splitting peaks in the absorption spectra of La-

substituted NdAlO₃. Hence, we report the tuning of f-orbital mediated crystal field splitting via substitution mechanism in La; NdAlO₃.

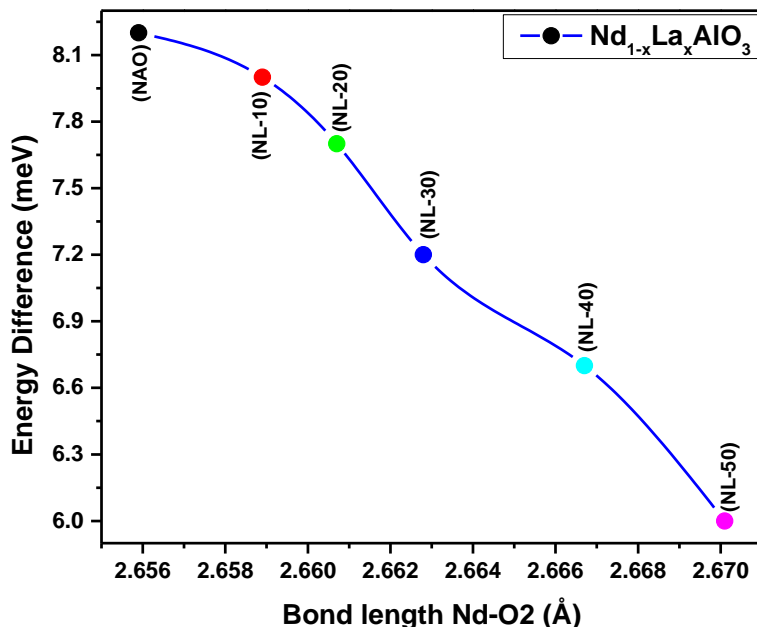


Figure 3.6: Energy difference ($\Delta E = E_2 - E_1$) vs bond length (Nd/La-O₂).

In **Figure 3.6**, the relationship between the energy difference (Transition Energy) ($\Delta E = E_2 - E_1$) and the bond length (Nd/La-O₂) is analysed. It is observed that as the La concentration increases on the Nd site in Nd_{1-x}La_xAlO₃ ($x = 0, 10, 20, 30, 40, 50\%$), the energy difference corresponding to the nearest two peaks ($^4f_{3/2}$) decreases. This trend is correlated with the bond length of Nd/La-O₂. Specifically, the bond length Nd/La-O₂ increases as the La concentration increases.

The decreasing energy difference ($^4f_{3/2}$) with increasing bond length suggests that the energy of the Nd ions in NdAlO₃ can be tuned by selectively doping La. The experimental observations align with the theoretical calculations performed using the PyCrystalfield software, as discussed in Chapter 4 of the study. This analysis provides valuable insights

into the impact of La substitution on the electronic structure and energy levels of the Nd ions in the $\text{Nd}_{1-x}\text{La}_x\text{AlO}_3$ system.

Chapter-4:

Theoretical Work:

In this chapter, we explore various aspects related to the crystal field theory and its application in tuning the crystal field energy by selectively choosing materials. Firstly, we discuss the crystal field Hamiltonian, which describes the interaction between the transition metal or rare-earth ion and its surrounding ligands in a crystal field environment. The Hamiltonian provides a mathematical framework to analyze the splitting of energy levels and the corresponding electronic transitions.

Next, we delve into the matrix element formula, which allows us to calculate the transition probabilities between different energy levels in the crystal field. This formula considers the wavefunctions and symmetries of the initial and final states, providing insights into the intensity and selection rules of optical transitions.

Furthermore, we introduce the PyCrystalfield software, which is a computational tool used to simulate and analyze crystal field transitions in complex materials. This software enables us to calculate energy level diagrams, transition probabilities, and other properties related to crystal field interactions. By utilizing PyCrystalfield, we can gain a deeper understanding of the effects of different ligand environments and dopants on the crystal field energy levels.

Finally, we discuss the correlation between the energy level splitting and bond length in the crystal lattice. By selectively choosing materials with specific bond lengths, we can effectively tune the crystal field energy. Through experimental and theoretical investigations, we aim to demonstrate how the crystal field energy can be decreased by increasing the bond length,

providing insights into the design and synthesis of materials with tailored optical and electronic properties.

4.1: Theoretical model:

Crystal field potential of Nd^{3+} : The complex energy level schemes of the Nd^{3+} ion in the crystal result from several interactions both within the $4f^3$ electron configuration and between the Nd^{3+} ion and its environment. The Parametric Model Hamiltonian used in this study can be written as:²²

$$H = H_A + H_{CF} \quad (4.1)$$

Where H_A stands for the atomic Hamiltonian and is the H_{CF} crystal-field interaction Hamiltonian. The H_A operator can be written as:²²

$$H_A = E_{avg} + \sum_{k=2,4,6} F^k f_k + \xi A_{SO} + \alpha L(L+1) + \beta G(G_2) + \gamma G(R_7) \\ + \sum_{i=2,3,4,6,7,8} T^i t_i + \sum_{j=0,2,4} M^j m_j + \sum_{k=2,4,6} P^k p_k \quad (4.2)$$

In this expression, the parameter E_{avg} is the spherically symmetric one-electron part of the Hamiltonian. The electrostatic interaction is described with the Slater integrals $F^k f_k$ ($k = 2, 4, \text{ and } 6$), where F^k and f_k are the radial part and the angular part, respectively. ξ and A_{SO} are the radial part and the angular part of spin-orbit interaction, respectively. α , β and γ are two-body electrostatic parameters, $G(G_2)$ and $G(R_7)$ are Casimir operators for the G_2 and R_7 groups, and L is the total orbital angular-momentum. $T^i t_i$ ($i = 2, 3, 4, 6, 7$ and 8) describes the three-body configuration interaction, where T^i is parameter and t_i is an operator. Higher-order magnetic spin-spin and spin-other-orbit interactions as well as the electrostatically correlated spin-orbit interactions can be represented

by Marvin integrals M^j ($j = 0, 2, \text{ and } 4$) and P^k ($k = 2, 4, \text{ and } 6$), and the operators associated with these parameters are designated by m_j and p_k , respectively.^{68,69,22}

We know, Crystal field interaction refers to the perturbation or distortion of the electron cloud surrounding a central rare earth ion caused by its surrounding ligands. The ligands, which can be atoms, ions, or molecules, interact with the central ion through electrostatic forces. These forces arise from the electric fields generated by the charges on the ligands. The presence of ligands around the central rare earth ion disrupts the spherical symmetry of its electron cloud, leading to a distortion in the energy levels of the ion's electronic configuration. This distortion is a consequence of the different electrostatic interactions between the electrons and the ligands. The ligands can attract or repel the electrons, causing the energy levels to split and giving rise to crystal field splitting.

The crystal field Hamiltonian H_{CF} is defined as:

$$H_{CF} = -e \sum_{i=1}^n V(r_i) \quad (4.3)$$

Where $V(r_i)$ represents the potential felt by an electron at a specific position described by the position vector of electron r_i . The sum is taken over all electrons in the system, from $i = 1$ to n . The term $-e$ represents the elementary charge, which is a fundamental constant representing the charge of an electron.

If crystal field perturbation affects the $4f^n$ electrons, the potential can be expressed using the following equation:

$$V(r_i) = \int \frac{\rho(R) dV}{|R-r_i|} \quad (4.4)$$

In the equation, dV represents the volume element within the crystal lattice. R denotes the position vector within the lattice, which describes the

location of a specific point within the crystal. $\rho(R)$ represents the charge distribution, which refers to the spatial distribution of electric charges within the crystal lattice.

The potential in eqⁿ. (4.2) can be expanded using the expression.

$$\frac{1}{|R - r_i|} = \sum_{k=0}^{\infty} \left(\frac{r_{<}^k}{r_{>}^{k+1}} P_k(\cos \omega) \right) \quad (4.5)$$

Where $P_k(\cos(\omega))$ are the Legendre polynomial, ω is the angle between R & r_i , $r_{<}$ is the smaller distance and $r_{>}$ is the larger distance of (r_i, R) .

If the charge distribution of the crystal does not penetrate that of the 4f electron, then we can assume $r_i < R$.

Thus, we can rewrite the equation as:

$$\frac{1}{|R - r_i|} = \sum_{k=0}^{\infty} \left(\frac{r_i^k}{R^{k+1}} P_k(\cos \omega) \right) \quad (4.6)$$

According to spherical harmonic addition theory (Griffith 1961)⁷⁰ $P_k(\cos \omega)$ has been expanded, which expressed the angle ω between R and r_i in term of polar angles (θ, φ) and (θ_i, φ_i) .

$$P_k(\cos \omega) = \frac{4\pi}{2k + 1} \sum_{q=-k}^{+k} Y_k^{q*}(\theta, \varphi) Y_k^q(\theta_i, \varphi_i) \quad (4.7)$$

Where (θ, φ) is angular distribution of charge and (θ_i, φ_i) is angular position of electron i . Y_k^q is spherical harmonica. The value of Y_k^q for $k=0,1,2,3,4,5,6,7$ is available in literature.

$$Y_k^{q*}(\theta, \varphi) = (-1)^q Y_k^{-q}(\theta, \varphi) \quad (4.7A)$$

Where $Y_k^{q*}(\theta, \varphi)$ is the complex conjugate of $Y_k^{-q}(\theta, \varphi)$.

Now from equations (4.6) and (4.7A), we can rewrite.

$$P_k(\cos \omega) = \frac{4\pi}{2k+1} \sum_{q=-k}^{+k} (-1)^q Y_k^{-q}(\theta, \varphi) Y_k^q(\theta_i, \varphi_i) \quad (4.7B)$$

So here we will see to $Y_k^{-q}(\theta, \varphi)$ as expansion coefficient and the $Y_k^q(\theta_i, \varphi_i)$ as operators.

Now, we will again rewrite equation (4.7B) without summation.

$$P_k(\cos \omega) = \frac{4\pi}{2k+1} \left[Y_k^0(\theta, \varphi) Y_k^0[\theta_i, \varphi_i] + \sum_{q=1}^k (-1)^q \left(Y_k^{-q}(\theta, \varphi) Y_k^q(\theta_i, \varphi_i) + Y_k^q(\theta, \varphi) Y_k^{-q}(\theta_i, \varphi_i) \right) \right] \quad (4.7C)$$

Where the expansion coefficient $Y_k^0(\theta, \varphi)$ is real, but $Y_k^q(\theta, \varphi)$ and $Y_k^{-q}(\theta, \varphi)$ are complex quantities.

The equation (4.7c) can be expressed in terms of tesseral harmonic functions, and the relationship between tesseral and spherical harmonic functions is well-documented in the literature. The tesseral harmonic functions represent the angular part of the wave function in the crystal field Hamiltonian.

The relationship between tesseral and spherical harmonic functions is given by the following equation:

Tesseral harmonic function:

$$Z_{k0}^c = Y_k^0,$$

$$Z_{kq}^c = \frac{1}{\sqrt{2}} (Y_k^{-q} + (-1)^q Y_k^q),$$

$$Z_{kq}^c = \frac{i}{\sqrt{2}} (Y_k^{-q} - (-1)^q Y_k^q).$$

Where the superscripts c and s stand for the presence of the factors $\cos(q\varphi)$ and $\sin(q\varphi)$ in the tesseral harmonic.⁷⁰

Equation (4.8) can be rewritten as:

$$\begin{aligned}
 P_k(\cos \omega) = \frac{4\pi}{2k+1} & \left[z_{k0}^c Y_k^0[\theta_i, \varphi_i] \right. \\
 & + \sum_{q=1}^k \left(z_{kq}^c \frac{1}{\sqrt{2}} (Y_k^{-q}(\theta_i, \varphi_i) + (-1)^q Y_k^q(\theta_i, \varphi_i)) \right. \\
 & + z_{kq}^s \frac{i}{\sqrt{2}} (Y_k^{-q}(\theta_i, \varphi_i) \\
 & \left. \left. - (-1)^q Y_k^q(\theta_i, \varphi_i) \right) \right] \quad (4.8)
 \end{aligned}$$

Now above equation, we will write in short form.

Here, the spherical harmonic $Y_k^q(\theta_i, \varphi_i)$ will do replaced by the tensor operators $C_q^k(\theta_i, \varphi_i)$, which have same transformation properties as the spherical harmonics:

$$C_q^k(\theta_i, \varphi_i) = \sqrt{\frac{4\pi}{2k+1}} Y_k^q(\theta_i, \varphi_i).$$

So, we find.

$$\begin{aligned}
P_k(\cos \omega) = & \sqrt{\frac{4\pi}{(2k+1)}} \left[Z_{k0}^c C_0^k(\theta_i, \varphi_i) \right. \\
& + \sum_{q=1}^k (Z_{kq}^c \frac{1}{\sqrt{2}} (C_{-q}^k(\theta_i, \varphi_i) + (-1)^q C_q^k(\theta_i, \varphi_i)) \\
& + Z_{kq}^s \frac{i}{\sqrt{2}} (C_{-q}^k(\theta_i, \varphi_i) \\
& \left. - (-1)^q C_q^k(\theta_i, \varphi_i)) \right] \quad (4.9)
\end{aligned}$$

After combination of eq. (4.9) and eq. (4.4), put this value in eq. (4.2) and final crystal field potential is.

$$\begin{aligned}
V(r_i) &= \sum_{k=0}^{\infty} \sqrt{\frac{4\pi}{(2k+1)}} \left[Z_{k0}^c C_0^k(\theta_i, \varphi_i) \right. \\
& + \sum_{q=1}^k (Z_{kq}^c \frac{1}{\sqrt{2}} (C_{-q}^k(\theta_i, \varphi_i) + (-1)^q C_q^k(\theta_i, \varphi_i)) \\
& \left. + Z_{kq}^s \frac{i}{\sqrt{2}} (C_{-q}^k(\theta_i, \varphi_i) - (-1)^q C_q^k(\theta_i, \varphi_i)) \right] \\
& \times \int \rho(R) \frac{r_i^k}{R^{k+1}} dV \quad (4.10)
\end{aligned}$$

To simplify this expression, we introduce new coefficient B_0^k , B_q^k and $B_q'^k$:

$$B_0^k = \sqrt{\frac{4\pi}{2k+1}} Z_{k0}^c \int \rho(R) \frac{r^k}{R^{k+1}} dV,$$

$$B_0^k = \sqrt{\frac{4\pi}{2k+1}} \frac{Z_{kq}^c}{\sqrt{2}} \int \rho(R) \frac{r^k}{R^{k+1}} dV,$$

$$B_0'^k = \sqrt{\frac{4\pi}{2k+1}} \frac{Z_{kq}^s}{\sqrt{2}} \int \rho(R) \frac{r^k}{R^{k+1}} dV,$$

Here, B_q^k and $B_q'^k$ have $1/\sqrt{2}$ factor in the above expressions because B_q^k contains a cosine and $B_q'^k$ a sine part.

The eq. () can be rewritten in term of new coefficient B_0^k , B_q^k and $B_q'^k$ as:

$$V(r_i) = \sum_{k=0}^{\infty} \left[B_0^k C_0^k(\theta_i, \varphi_i) + \sum_{q=1}^k (B_q^k (C_{-q}^k(\theta_i, \varphi_i) + (-1)^q C_k^q(\theta_i, \varphi_i)) + B_q'^k \frac{i}{\sqrt{2}} (C_{-q}^k(\theta_i, \varphi_i) - (-1)^q C_k^q(\theta_i, \varphi_i))) \right] \quad (4.11)$$

So here, we will discuss for f systems $k = 0, 1, \dots, 7$. Now the crystal field potential V can be divided into an even ($k = \text{even}$) part and an odd part ($k = \text{odd}$). The even part of the crystal field potential is primarily responsible for the crystal field splitting, i.e., the energy level separation of the f orbitals. On the other hand, the odd part of the crystal field potential influences the intensity of induced electric dipole transitions. The value of q , which characterizes the odd part of the crystal field potential, is constrained by the point group symmetry of the rare earth site. The point group symmetry determines the allowed transitions and selection rules for the induced electric dipole transitions. Different point groups have different restrictions on the values of q , leading to variations in the intensity and nature of the electric dipole transitions.

From eq. (4.1) and (4.11), The Crystal field Hamiltonian is.

$$H_{CF} = -e \sum_{k=0}^{\infty} \left[B_0^k C_0^k(\theta_i, \varphi_i) + \sum_{q=1}^k (B_q^k (C_{-q}^k(\theta_i, \varphi_i) + (-1)^q C_k^q(\theta_i, \varphi_i)) + B_q'^k \frac{i}{\sqrt{2}} (C_{-q}^k(\theta_i, \varphi_i) - (-1)^q C_k^q(\theta_i, \varphi_i))) \right] \quad (4.12)$$

Example. For the D_3 symmetry of Nd^{+3} ion doped in perovskite structure crystal, the crystal-field Hamiltonian is expressed as follows:

In the Stevens Operator formalism, the D_3 symmetry gives six symmetries allowed CEF parameters: $B_0^2, B_0^4, B_3^4, B_3^4, B_0^6, B_3^6, B_6^6$.

The potential for the D_3 symmetric system is given by:

$$\begin{aligned} V^{even}(D_3) = & B_0^2 C_0^2(\theta_i, \varphi_i) + B_0^4 C_0^4(\theta_i, \varphi_i) + B_3^4 (C_{-3}^4(\theta_i, \varphi_i) - C_3^4(\theta_i, \varphi_i)) \\ & + B_0^6 C_0^6(\theta_i, \varphi_i) + B_3^6 (C_{-3}^6(\theta_i, \varphi_i) - C_3^6(\theta_i, \varphi_i)) \\ & + B_6^6 (C_{-6}^6(\theta_i, \varphi_i) + C_6^6(\theta_i, \varphi_i)) \end{aligned} \quad (4.13)$$

In this equation, $B_0^2, B_0^4, B_3^4, B_3^4, B_0^6, B_3^6,$ and B_6^6 are the CEF parameters corresponding to the respective terms in the potential. $C_q^k(\theta_i, \varphi_i)$ represents the Stevens operator coefficients, which depend on the polar angles (θ_i, φ_i) that define the position of the electron i . The potential consists of terms with different powers of k and q , and the ellipsis (...) represents additional terms that can be present in the potential.

This equation describes the potential energy experienced by the Nd^{+3} ion in a D_3 symmetric crystal field environment. The specific values of the CEF parameters $(B_0^2, B_0^4, B_3^4, B_3^4, B_0^6, B_3^6, B_6^6)$ determine the shape and energy levels of the crystal field splitting for the Nd^{+3} ion in this system.

Crystal field parameters and Crystal field matrix elements:

The crystal field energy levels can be determined by diagonalizing the crystal field matrix, which is obtained from the expectation values of the crystal field Hamiltonian. The expectation value of the crystal field Hamiltonian can be expressed as:

$$\begin{aligned} & \langle \psi_{nlm} | H_{CF} | \psi_{nlm} \rangle \\ = & \left\langle \psi_{nlm} \left| -e \sum_{k=0}^{\infty} \left[\begin{aligned} & B_0^2 C_0^2(\theta_i, \varphi_i) + B_0^4 C_0^4(\theta_i, \varphi_i) + B_3^4 (C_{-3}^4(\theta_i, \varphi_i) - C_3^4(\theta_i, \varphi_i)) + \\ & B_0^6 C_0^6(\theta_i, \varphi_i) + B_3^6 (C_{-3}^6(\theta_i, \varphi_i) - C_3^6(\theta_i, \varphi_i)) + B_6^6 (C_{-6}^6(\theta_i, \varphi_i) + C_6^6(\theta_i, \varphi_i)) \end{aligned} \right] \right| \psi_{nlm} \right\rangle \end{aligned} \quad (4.14)$$

In this equation, $|\psi_{nlm}\rangle$ represents the wavefunction corresponding to the electronic state with quantum numbers n , l , and m . The crystal field Hamiltonian consists of terms involving crystal field parameters B_0^k , B_q^k and $B_q'^k$, as well as the spherical harmonics $C_{-q}^k(\theta_i, \varphi_i)$ and $C_k^q(\theta_i, \varphi_i)$ that depend on the angles θ_i and φ_i .

The crystal field parameters B_0^k , B_q^k and $B_q'^k$ describe the strength of the crystal field interactions and depend on the specific symmetry of the crystal field potential. The terms involving these parameters contribute to the splitting of the energy levels.

The spherical harmonics $C_{-q}^k(\theta_i, \varphi_i)$ and $C_k^q(\theta_i, \varphi_i)$ represent the angular dependence of the wavefunction and depend on the polar angle θ_i and azimuthal angle φ_i . These terms account for the orientation of the electronic orbitals in the crystal field potential and influence the energy levels of the system.

PyCrystalfield Software:

In this study, we introduced PyCrystalfield, a Python software package specifically designed for calculating single-ion crystal electric field (CEF) Hamiltonians. The software allows for the computation of crystal field parameters such as eigenvalues and eigenvectors.

PyCrystalfield operates based on the crystal electric field Hamiltonian, which considers the interaction between the transition metal or rare-earth ion and its surrounding ligands. By treating the ligands as point charges and considering the Coulombic repulsion between them, the CEF Hamiltonian can be determined.

Using PyCrystalfield, researchers can obtain valuable insights into the electronic structure and energy level splitting of complex materials. The software facilitates the calculation of CEF Hamiltonians, which in turn enable the determination of crystal field parameters for a given system.

These parameters play a crucial role in understanding and predicting various properties, including magnetic behaviour, optical transitions, and spectroscopic features.

By utilizing PyCrystalfield, scientists can effectively model and analyze the crystal field interactions in materials, allowing for a better understanding of their electronic and optical properties. The software provides a valuable tool for researchers working in the field of solid-state physics and materials science, aiding in the design and characterization of novel materials with tailored functionalities.

The general CEF Hamiltonian is:

$$H_{CEF} = \sum B_n^m O_n^m \dots\dots\dots (5.1)$$

Where O_n^m are the Stevens operators (Stevens, 1952; Hutchings, 1964) and B_n^m are the multiplicative factors called CEF parameters. ‘n’ is the operator degree and is constrained by time-reversal symmetry to be even (Newman, 1971). ‘m’ is the operators order, and $-n \geq m \geq n$. These parameters can either be fit to experimental data or calculate from a point charge model approximation as a starting point of the fit.

The calculation of B_n^m has been using the method outlined by Hutchings (1964),

Where Point charge model.

$$B_n^m = -\gamma_{nm} q C_{nm} \langle r^n \rangle \theta_n \dots\dots\dots (5.2)$$

Here, γ_{nm} is a term calculated from the ligand environment expressed in term of tesseral harmonics, q is the charge of the central ion (in unit of e), C_{nm} are normalization factors of the spherical harmonics, $\langle r^n \rangle$ is the expectation value of the radial wavefunction (taken from Edvarsson (1998) for all rare earth ions), and θ_n is a multiplicative factor which is dependent on the ion ($\theta_2 = \alpha_j; \theta_4 = \beta_j; \theta_6 = \gamma_j$). When calculating crystal field

levels from the B_n^m , the θ_n constants are listed in Stevens (1952) for ground states of all the rare earth ions in the J basis.

Implementation:

Relation between ligands and CF Levels objects:

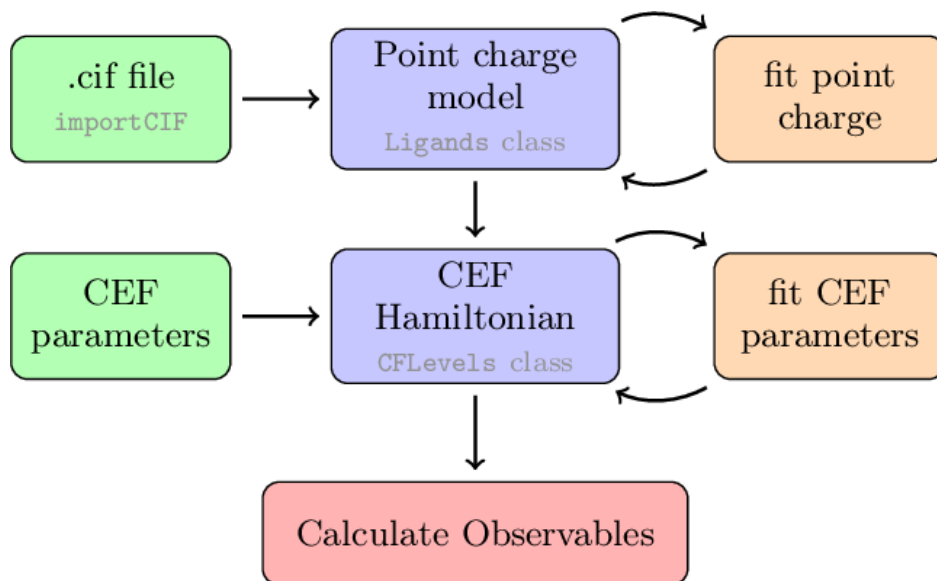


Figure 5.1: PyCrystalfield workflow. One can begin either with a .cif file or a list of CEF parameters, and then calculate a point charge model or a CEF Hamiltonian respectively.

Example: For NdAlO₃ perovskite material, the eigen value has been calculated by PyCrystalfield Software:

Energy level of ground state of Nd⁺³ in Nd_{1-x}La_xAlO₃ sample:

The energy level of ground state of f-orbitals (Nd⁺³ with La-substitution) for all sample has been calculated by PyCrystalfield software. The energy level of Nd⁺³ for ground state f-orbitals in Nd_{1-x}La_xAlO₃ (x=0,0.1,0.2,0.3,0.4,0.5) is listed in table (5.1).

Table 4.1: Ground state energy of Nd-ions.

Energy Level of Nd ⁺³ in NLAO	X=0	X=0.1	X=0.2	X=0.3	X=0.4	X=0.5
	0	0	0	0	0	0
	0	0	0	0	0	0
	7.837	6.237	4.500	3.427	4.068	4.226
	7.837	6.237	4.500	3.427	4.068	4.226
	10.631	9.559	8.505	7.927	8.289	8.393
	10.631	9.559	8.505	7.927	8.289	8.393
	37.787	36.037	34.325	33.296	33.512	33.407
	37.787	36.037	34.325	33.296	33.512	33.407
	39.341	37.293	35.217	33.947	34.376	34.354
	39.341	37.293	35.217	33.947	34.376	34.354

Table 4.2: The relation between change transition energy and bond length.

Nd _{1-x} La _x AlO ₃	Change Transition Energy (meV)	Bond Length (Nd/La-O)
X=0	27.156	2.6559(8)

X=10	26.477	2.6589(7)
X=20	25.819	2.6607(8)
X=30	25.369	2.6628(8)
X=40	25.220	2.6667(9)
X=50	25.010	2.6701(7)

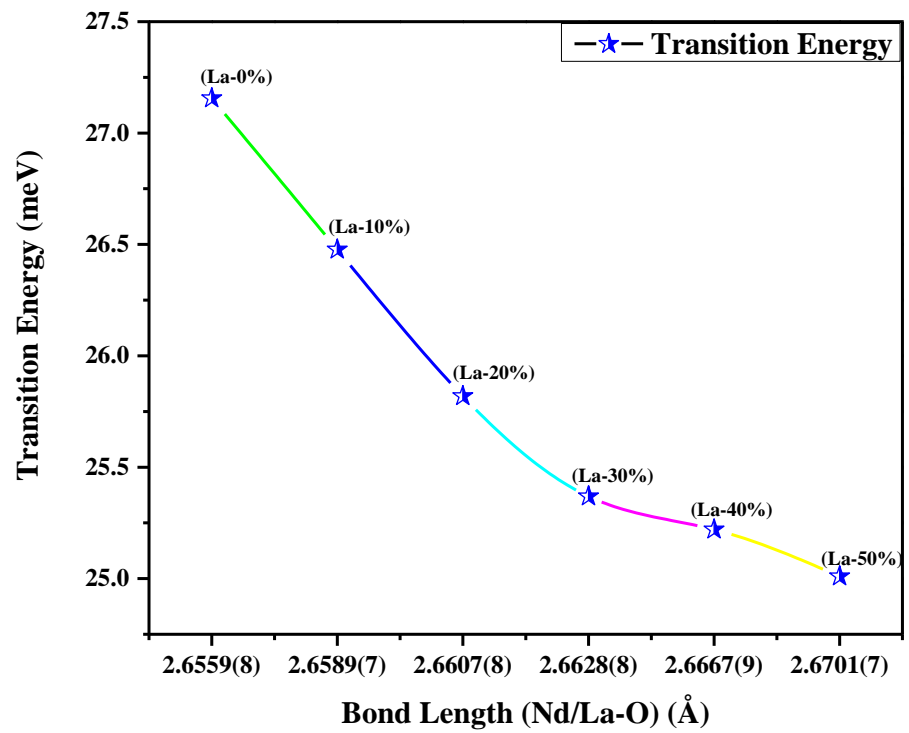


Figure 5.2: Variation of transition energy with bond length (Nd/La-O).

The bond length Nd/La-O for $\text{Nd}_{1-x}\text{La}_x\text{AlO}_3$ ($x=0,10,20,30,40,50\%$) has been observed in increasing mode and it has been correlated with transition energy in the present of magnetic field and electrostatics field

that which is decreasing with bond length. So, we can say that the energy of Nd in NdAlO₃ by selective dopant can be tuned.

Chapter 5

Summary and Future plans:

5.1 Summary of the work:

❖ *Sample preparation:* Sample synthesis has been carried out via Sol-gel method

❖ *X-Ray Diffraction:* Phase purity has been characterized through X-ray diffraction technique and crystallographic information has been obtained via Rietveld refinement. VESTA software was used to extract the values of Nd-O₂ bond lengths.

❖ *Optical Absorption Spectroscopy:* The signature of crystal field transitions in NAO samples due to unpaired *f*-electrons has been observed via the optical absorption spectroscopy in diffused reflectance mode and PyCrystalfield software. The corresponding energy difference between two adjacent transition peaks is found to systematically decrease with increase in La-concentration in the Nd_{1-x}La_xAlO₃.

❖ *Correlation of crystal field transitions with Nd-O bond length:* The Decrease in difference of the transition energy can be correlated with Nd/La-O Bond length, attributing to the reduced effective overlapping between of Nd and O ions

Future Scope

❖ To understand a more accurate description, advanced computational methods like density function theory (DFT) can be employed, which considers the electron density distribution and its interaction with the ligands and the Nd^{+3} ion.

❖ Raman spectroscopy measurement to understand lattice vibrations and their correlation with structural and optical properties.

Reference:

- (1) Bati, A. S. R.; Zhong, Y. L.; Burn, P. L.; Nazeeruddin, M. K.; Shaw, P. E.; Batmunkh, M. Next-Generation Applications for Integrated Perovskite Solar Cells. *Commun. Mater.* **2023**, *4* (1), 1–24. <https://doi.org/10.1038/s43246-022-00325-4>.
- (2) Perovskite (Structure). *Wikipedia*; 2023.
- (3) (2) Bilal Hanif, M.; Motola, M.; qayyum, S.; Rauf, S.; khalid, A.; Li, C.-J.; Li, C.-X. Recent Advancements, Doping Strategies and the Future Perspective of Perovskite-Based Solid Oxide Fuel Cells for Energy Conversion. *Chem. Eng. J.* **2022**, *428*, 132603. <https://doi.org/10.1016/j.cej.2021.132603>.
- (4) *Metal Halide Perovskite Nanocrystals: Synthesis, Post-Synthesis Modifications, and Their Optical Properties | Chemical Reviews.* <https://pubs.acs.org/doi/10.1021/acs.chemrev.8b00644> (accessed 2023-06-01).
- (5) Applications of Photovoltaics. *Wikipedia*; 2023.
- (6) *PEROVSKITE CELLS IN THE FUTURE OF PHOTOVOLTAICS.* Pinterest. <https://www.pinterest.com/pin/perovskite-cells-in-the-future-of-photovoltaics--637963103459872919/> (accessed 2023-05-22).
- (7) Xu, X.; Pan, Y.; Zhong, Y.; Ran, R.; Shao, Z. Ruddlesden–Popper Perovskites in Electrocatalysis. *Mater. Horiz.* **2020**, *7* (10), 2519–2565. <https://doi.org/10.1039/D0MH00477D>.
- (8) Zhang, H.; Li, N.; Li, K.; Xue, D. Structural Stability and Formability of ABO₃-Type Perovskite Compounds. *Acta Crystallogr. B* **2007**, *63* (6), 812–818. <https://doi.org/10.1107/S0108768107046174>.
- (9) Gupta, M.; Rambadey, O. V.; Sagdeo, P. R. Probing the Effect of R-Cation Radii on Structural, Vibrational, Optical, and Dielectric Properties of Rare Earth (R= La, Pr, Nd) Aluminates. *Ceram. Int.* **2022**, *48* (16), 23072–23080.
- (10) Zhu, L.; Ran, R.; Tadé, M.; Wang, W.; Shao, Z. Perovskite Materials in Energy Storage and Conversion. *Asia-Pac. J. Chem. Eng.* **2016**. <https://doi.org/10.1002/apj.2000>.

- (11) Peña-Martínez, J.; Marrero-López, D.; Ruiz-Morales, J. C.; Buergler, B. E.; Núñez, P.; Gauckler, L. J. *Fuel Cell Studies of Perovskite-Type Materials for IT-SOFC*. *J. Power Sources* **2006**, *159* (2), 914–921. <https://doi.org/10.1016/j.jpowsour.2005.11.036>.
- (12) *Journal of Magnetism and Magnetic Materials* | Vol 514, 15 November 2020 | ScienceDirect.com by Elsevier. <https://www.sciencedirect.com/journal/journal-of-magnetism-and-magnetic-materials/vol/514/suppl/C> (accessed 2023-01-10).
- (13) Sati, A.; Pokhriyal, P.; Kumar, A.; Anwar, S.; Sagdeo, A.; Lalla, N. P.; Sagdeo, P. R. *Origin of Ferroelectricity in Cubic Phase of Hf Substituted BaTiO₃*. *J. Phys. Condens. Matter Inst. Phys. J.* **2021**, *33* (16). <https://doi.org/10.1088/1361-648X/abf0bf>.
- (14) He, J.; Liu, Z.; Cao, Z.; Zhang, H.; Meng, Y.; Chen, B.; Zhong, D. Visualizing the Redox Reaction Dynamics of Perovskite Nanocrystals in Real and Reciprocal Space. *J. Phys. Chem. Lett.* **2020**, *11* (7), 2550–2558. <https://doi.org/10.1021/acs.jpcclett.0c00265>.
- (15) *abo₃ perovskite*. Bing. <https://www.bing.com/images/search?q=abo3+perovskite&id=029601218D98F8C85098B1E302ADB1C0AE16648&FORM=IQFRBA> (accessed 2023-05-22).
- (16) Howard, C. J.; Kennedy, B. J.; Chakoumakos, B. C. Neutron Powder Diffraction Study of Rhombohedral Rare-Earth Aluminates and the Rhombohedral to Cubic Phase Transition. *J. Phys. Condens. Matter* **2000**, *12* (4), 349. <https://doi.org/10.1088/0953-8984/12/4/301>.
- (17) Yao, J.; Chen, T.; Wang, H.; Khan, M.; Tan, C.; Sun, Y.; Su, W.; Wang, H.; Wang, C. Stable Cubic Crystal Structures and Optimized Thermoelectric Performance of SrTiO₃-Based Ceramics Driven by Entropy Engineering. *J. Mater. Chem. A* **2022**, *10* (46), 24561–24572. <https://doi.org/10.1039/D2TA06576B>.
- (18) Luo, X.; Wang, B. Structural and Elastic Properties of LaAlO₃ from First-Principles Calculations. *J. Appl. Phys.* **2008**, *104* (7), 073518. <https://doi.org/10.1063/1.2990068>.
- (19) *Wybourne: Spectroscopic properties of rare earths - Google Scholar*. https://scholar.google.com/scholar_lookup?title=Spectroscopic%20Properties%20of%20Rare%20Earths&publication_year=1965&author=B.G.%20Wybourne (accessed 2023-05-23).
- (20) Huang, P.; Zheng, W.; Gong, Z.; You, W.; Wei, J.; Chen, X. Rare Earth Ion- and Transition Metal Ion-Doped Inorganic Luminescent Nanocrystals: From

Fundamentals to Biodetection. *Mater. Today Nano* **2019**, *5*, 100031.

<https://doi.org/10.1016/j.mtnano.2019.100031>.

(21) Wang, J.; Wang, F.; Luo, Y.; Li, X.; Jia, Y. Improved the Stability and Enhanced Luminescence of Er Doped CsPbBr₃ Perovskite. *Mater. Sci. Semicond. Process.* **2022**, *151*, 107021. <https://doi.org/10.1016/j.mssp.2022.107021>.

(22) Christiane Gorller-Walrand, K. B. RATIONALIZATION OF CRYSTAL-FIELD PARAMETRIZATION. In *Handbook on the physics and chemistry of Rare Earths*; Elsevier Science B.V.: Belgium, 1996; Vol. 23.

(23) Howard, C. J.; Kennedy, B. J.; Chakoumakos, B. C. Neutron Powder Diffraction Study of Rhombohedral Rare-Earth Aluminates and the Rhombohedral to Cubic Phase Transition. *J. Phys. Condens. Matter* **2000**, *12* (4), 349. <https://doi.org/10.1088/0953-8984/12/4/301>.

(24) Gupta, M.; Rambadey, O. V.; Sagdeo, P. R. Probing the Effect of R-Cation Radii on Structural, Vibrational, Optical, and Dielectric Properties of Rare Earth (R=La, Pr, Nd) Aluminates. *Ceram. Int.* **2022**, *48* (16), 23072–23080. <https://doi.org/10.1016/j.ceramint.2022.04.285>.

(25) Li, J.; Qiu, T. Synthesis and Characterization of SmAlO₃ Dielectric Material by Citrate Precursor Method. *J. Sol-Gel Sci. Technol.* **2012**, *61* (1), 112–118. <https://doi.org/10.1007/s10971-011-2598-1>.

(26) Tkachenko, N. V. *Optical Spectroscopy: Methods and Instrumentations*; Elsevier, 2006.

(27) 9.1: Crystal Field Theory. Chemistry LibreTexts. https://chem.libretexts.org/Courses/East_Tennessee_State_University/CHEM_3110%3A_Descriptive_Inorganic_Chemistry/09%3A_Coordination_Chemistry-_Bonding/9.01%3A_Crystal_Field_Theory (accessed 2023-05-23).

(28) Görller-Walrand, C.; Binnemans, K. Chapter 155 Rationalization of Crystal-Field Parametrization. In *Handbook on the Physics and Chemistry of Rare Earths*; Elsevier, 1996; Vol. 23, pp 121–283. [https://doi.org/10.1016/S0168-1273\(96\)23006-5](https://doi.org/10.1016/S0168-1273(96)23006-5).

(29) Xu, C.; Yang, C.; Zhu, H.; Ye, Y.; Duan, Y.; Wei, P.; Zhang, H.; Zhang, J.; Tang, D. Diode-Pumped Nd:LuAG Ceramic Laser on 4F_{3/2}-4I_{13/2} transition. *Opt. Mater.* **2017**, *71*, 121–124. <https://doi.org/10.1016/j.optmat.2016.04.021>.

(30) Liu, G.; Wang, B.; Li, J.; Cao, B.; Lu, Y.; Liu, Z. Research Progress of Gadolinium Aluminum Garnet Based Optical Materials. *Phys. B Condens. Matter* **2021**, *603*, 412775. <https://doi.org/10.1016/j.physb.2020.412775>.

- (31) Sriram, D.; Jayaprakash, G.; Arulkirubakaran, D.; Prabu, M.; Ajithkumar, A. Laser Turning of Alumina (Al₂O₃) Ceramic by Nd:YAG Laser Technique. *Mater. Today Proc.* **2021**, *39*, 731–735. <https://doi.org/10.1016/j.matpr.2020.09.405>.
- (32) Gruber, J. B.; Hills, M. E.; Allik, T. H.; Jayasankar, C. K.; Quagliano, J. R.; Richardson, F. S. Comparative Analysis of Nd³⁺(4f³) Energy Levels in Four Garnet Hosts. *Phys. Rev. B* **1990**, *41*, 7999–8012. <https://doi.org/10.1103/PhysRevB.41.7999>.
- (33) Ezaki, M.; Obara, M.; Kumagai, H.; Toyoda, K. Characterization of Nd:Y₃Al₅O₁₂ Thin Films Grown on Various Substrates by Pulsed Laser Deposition. *Appl. Phys. Lett.* **1996**, *69* (20), 2977–2979. <https://doi.org/10.1063/1.117749>.
- (34) *Laser Plasma Division, RRCAT.*
https://www.rrcat.gov.in/technology/laser/lpd/xray_diffraction.html (accessed 2023-06-01).
- (35) *Goldschmidt tolerance factor (t) of various perovskite materials. [5].* ResearchGate. https://www.researchgate.net/figure/Goldschmidt-tolerance-factor-t-of-various-perovskite-materials-5_tbl1_334608582 (accessed 2023-05-24).
- (36) Sato, T.; Takagi, S.; Deledda, S.; Hauback, B. C.; Orimo, S. Extending the Applicability of the Goldschmidt Tolerance Factor to Arbitrary Ionic Compounds. *Sci. Rep.* **2016**, *6* (1), 23592. <https://doi.org/10.1038/srep23592>.
- (37) Scott, J. F. Raman Study of Trigonal-Cubic Phase Transitions in Rare-Earth Aluminates. *Phys. Rev.* **1969**, *183* (3), 823–825. <https://doi.org/10.1103/PhysRev.183.823>.
- (38) Maciel, G. S.; Rakov, N.; Zanon, R. A. D. S.; Fellows, C. E.; Guimarães, R. B.; Rodrigues, J. J. Red Photoluminescence in NdAlO₃ Crystalline Ceramic Powders Prepared by Combustion Synthesis. *Chem. Phys. Lett.* **2008**, *465* (4–6), 258–260. <https://doi.org/10.1016/j.cplett.2008.09.062>.
- (39) Dionicio-Navarrete; Arrieta-Gonzalez; Quinto-Hernandez; Casales-Diaz; Zuñiga-Diaz; Porcayo-Calderon; Martinez-Gomez. Synthesis of NdAlO₃ Nanoparticles and Evaluation of the Catalytic Capacity for Biodiesel Synthesis. *Nanomaterials* **2019**, *9* (11), 1545. <https://doi.org/10.3390/nano9111545>.
- (40) Ishihara, T.; Matsuda, H.; Mizuhara, Y.; Takita, Y. Improved Oxygen Ion Conductivity of NdAlO₃ Perovskite-Type Oxide by Doping with Ga. *Solid State Ion.* **1994**, *70–71*, 234–238. [https://doi.org/10.1016/0167-2738\(94\)90316-6](https://doi.org/10.1016/0167-2738(94)90316-6).
- (41) Maciel, G. S.; Rakov, N.; Zanon, R. A. D. S.; Fellows, C. E.; Guimarães, R. B.; Rodrigues, J. J. Red Photoluminescence in NdAlO₃ Crystalline Ceramic

Powders Prepared by Combustion Synthesis. *Chem. Phys. Lett.* **2008**, *465* (4–6), 258–260. <https://doi.org/10.1016/j.cplett.2008.09.062>.

(42) Strek, W.; Marciniak, L.; Hreniak, D.; Lukowiak, A. Anti-Stokes Bright Yellowish Emission of NdAlO₃ Nanocrystals. *J. Appl. Phys.* **2012**, *111* (2), 024305. <https://doi.org/10.1063/1.3674272>.

(43) Charles Kittel-8th Edition. *Introduction to Solid State Physics*.

(44) Strek, W.; Marciniak, L.; Hreniak, D.; Lukowiak, A. Anti-Stokes Bright Yellowish Emission of NdAlO₃ Nanocrystals. *J. Appl. Phys.* **2012**, *111* (2), 024305. <https://doi.org/10.1063/1.3674272>.

(45) Fig. 3. Crystal structure of perovskite ABO₃; A(Yellow), B(Black),... ResearchGate. https://www.researchgate.net/figure/Crystal-structure-of-perovskite-ABO3-AYellow-BBlack-OWhite_fig1_313460045 (accessed 2023-05-24).

(46) Fig. 2. Optical absorption spectrum of 1 at% Nd: YAG ceramic. ResearchGate. https://www.researchgate.net/figure/Optical-absorption-spectrum-of-1-at-Nd-YAG-ceramic_fig2_2974431 (accessed 2023-05-24).

(47) Study of Nd³⁺ ion as a Dopant in YAG and Glass Laser. <http://pubs.sciepub.com/ijp/1/1/3/> (accessed 2023-05-24).

(48) Fig. 3 Description of the splitting of f-orbitals of Tm³⁺ in O_h and... ResearchGate. https://www.researchgate.net/figure/Description-of-the-splitting-of-f-orbitals-of-Tm-3-in-O-h-and-D-3-configurations-and_fig3_294108382 (accessed 2023-05-24).

(49) Barnes, N. P.; Walsh, B. M.; Hutcheson, R. L.; Equall, R. W. Pulsed ⁴F_{3/2} to ⁴I_{9/2} Operation of Nd Lasers. *JOSA B* **1999**, *16* (12), 2169–2177. <https://doi.org/10.1364/JOSAB.16.002169>.

(50) Sol Gel Synthesis Routes. Processes are defined as sol-gel by the... ResearchGate. https://www.researchgate.net/figure/Sol-Gel-Synthesis-Routes-Processes-are-defined-as-sol-gel-by-the-transition-of-colloidal_fig12_290797153 (accessed 2023-05-24).

(51) Khan, H.; Yerramilli, A. S.; D'Oliveira, A.; Alford, T. L.; Boffito, D. C.; Patience, G. S. Experimental Methods in Chemical Engineering: X-Ray Diffraction Spectroscopy—XRD. *Can. J. Chem. Eng.* **2020**, *98* (6), 1255–1266. <https://doi.org/10.1002/cjce.23747>.

(52) X-ray | Definition, History, & Facts | Britannica. <https://www.britannica.com/science/X-ray> (accessed 2023-05-24).

- (53) Prabhu, S.; Naveen, D. K.; Bangera, S.; Bhat, B. S. Production of X-RAYS Using X-RAY Tube. *J. Phys. Conf. Ser.* **2020**, *1712* (1), 012036. <https://doi.org/10.1088/1742-6596/1712/1/012036>.
- (54) Gupta, M.; Rambadey, O. V.; Sagdeo, A.; Sagdeo, P. R. Investigating the Structural, Vibrational, Optical, and Dielectric Properties in Mg-Substituted LaAlO₃. *J. Mater. Sci. Mater. Electron.* **2022**, *33* (16), 13352–13366. <https://doi.org/10.1007/s10854-022-08273-y>.
- (55) *Figure 3.3: Diffraction diagram illustrating Bragg's Law. The incident...* ResearchGate. https://www.researchgate.net/figure/Diffraction-diagram-illustrating-Braggs-Law-The-incident-X-rays-diffract-from-the_fig12_265941365 (accessed 2023-05-24).
- (56) AsAChemicalEngineer. *Schematic of an X-Ray Diffractometer.* r/ScienceImages. www.reddit.com/r/ScienceImages/comments/2mzcvw/schematic_of_an_xray_diffractometer/ (accessed 2023-05-24).
- (57) Myrick, M. L.; Simcock, M. N.; Baranowski, M.; Brooke, H.; Morgan, S. L.; McCutcheon, J. N. The Kubelka-Munk Diffuse Reflectance Formula Revisited. *Appl. Spectrosc. Rev.* **2011**, *46* (2), 140–165. <https://doi.org/10.1080/05704928.2010.537004>.
- (58) *Figure 1: A schematic comparing specular and diffuse reflections.* ResearchGate. https://www.researchgate.net/figure/A-schematic-comparing-specular-and-diffuse-reflections_fig4_309136628 (accessed 2023-05-24).
- (59) Gupta, M.; Rambadey, O. V.; Shirbhate, S. C.; Acharya, S.; Sagdeo, A.; Sagdeo, P. R. Probing the Signature of Disorder and Delocalization of Oxygen Vacancies and Anti-Site Defects in Doped LaAlO₃ Solid Electrolytes. *J. Phys. Chem. C* **2022**, *126* (48), 20251–20262.
- (60): *Experimental set up for diffuse reflectance measurement, (a) Carry 60 UV-Visible Spectrometer, (b) Internal set up of UV-Visible spectrometer.*
- (61) Nandi, S. *RAMAN SPECTROSCOPY*; 2021. <https://doi.org/10.13140/RG.2.2.24191.33445>.
- (62) Rambadey, O. V.; Gupta, M.; Sagdeo, P. R. Phonon-Mode-Specific Lattice Dynamical Coupling of Carriers in Semiconductors Using Raman and Optical Spectroscopic Techniques. *Phys. Rev. B* **2022**, *106* (7), 075204.
- (63) Rambadey, O. V.; Kumar, A.; Sagdeo, P. R. Investigating the Correlation between the Urbach Energy and Asymmetry Parameter of the Raman Mode in Semiconductors. *Phys. Rev. B* **2021**, *104* (24), 245205.

- (64) Kumar, A.; Rambadey, O. V.; Rai, H.; Sagdeo, P. R. Role of Laser Excitation Wavelength and Power in the Fano Resonance Scattering in RFeO₃. 50CrO₃. 50O₃ (R= Sm, Er, and Eu): A Brief Raman Study. *J. Phys. Chem. C* **2022**, *126* (12), 5403–5410.
- (65) staff. *Raman Spectroscopy*. Science Facts. <https://www.sciencefacts.net/raman-spectroscopy.html> (accessed 2023-05-24).
- (66) Karati, A. *Rietveld Refinement Using FullProf Software*; 2018.
- (67) Momma, K.; Izumi, F. VESTA 3 for Three-Dimensional Visualization of Crystal, Volumetric and Morphology Data. *J. Appl. Crystallogr.* **2011**, *44* (6), 1272–1276. <https://doi.org/10.1107/S0021889811038970>.
- (68) Karbowiak, M.; Edelstein, N. M.; Droz, J. Spectroscopic Studies and Dynamics of Nd³⁺ Ions in RbY₂Cl₇ Single Crystals. Part II. Crystal-Field Analysis. *Chem. Phys.* **2002**.
- (69) Gao, J.; Zhang, Q.; Sun, D.; Luo, J.; Liu, W.; Yin, S. Energy Levels Fitting and Crystal-Field Calculations of Nd³⁺ Doped in GYSGG Crystal. *Opt. Commun.* **2012**, *285* (21), 4420–4426. <https://doi.org/10.1016/j.optcom.2012.06.050>.
- (70) Tikochinsky, Y. An Addition Theorem for Spherical Harmonics. *Math. Proc. Camb. Philos. Soc.* **1967**, *63* (4), 1093–1096. <https://doi.org/10.1017/S030500410004216X>.